

Contents lists available at ScienceDirect

Journal of the Mechanics and Physics of Solids

journal homepage: www.elsevier.com/locate/jmps





A model of void coalescence in columns

M.E. Torki ^{a,b}, F.A. Medrano ^b, A.A. Benzerga ^{b,c,*}, J.-B. Leblond ^d

- ^a School of Engineering and Applied Science, University of Pennsylvania, Philadelphia, PA 19104, USA
- ^b Department of Aerospace Engineering, Texas A&M University, College Station, TX 77843, USA
- ^c Department of Materials Science and Engineering, Texas A&M University, College Station, TX 77843, USA
- d Sorbonne Universites, UPMC Univ Paris 06, CNRS, UMR 7190, Institut Jean Le Rond d'Alembert, F-75005, Paris, France

ARTICLE INFO

Keywords: Ductile fracture Porous plasticity Strain localization Void growth Lode effects

ABSTRACT

Void coalescence in columns (or *necklace* coalescence) is a computationally confirmed and physically observed mechanism of void link-up in metal alloys and polymers that has received little attention in the literature. Here, analytical treatment of the phenomenon proceeds from first principles of limit analysis and homogenization theories. A cylindrical unit cell embedding a cylindrical void of finite height is considered under axially symmetric loading. Two types of trial velocity fields are used in seeking an upper bound to the yield criterion corresponding to the particular regime of coalescence in columns. For each type, exact expressions of the overall yield criterion are obtained, albeit in implicit form when using continuous fields. Upon comparison with other modes of yielding allowing for void growth and coalescence in layers, an actual effective yield domain is obtained so as to ascertain regimes of stress state and microstructural states where void coalescence in columns prevails. The predictions are also assessed against finite element based limit analysis.

1. Introduction

Modeling microvoid coalescence, the ultimate elementary stage of ductile fracture, has attracted much attention over the past few years. Benzerga and Leblond (2014) developed an effective yield criterion for a porous plastic solid in a "state of coalescence", improving upon an earlier semi-analytical model (Thomason, 1985). When supplemented with evolution equations for the microstructural variables, as in Benzerga (2002), and strain hardening, as in Gurson (1977) the constitutive relations are closed. Further developments subsequently aimed to incorporate the effect of resolved shear on the plane of coalescence (Torki et al., 2015, 2017), more accurate velocity fields in the underlying analysis (Morin et al., 2015), plastic anisotropy (Keralavarma and Chockalingam, 2016), a better account for the case of flat voids (Hure and Barrioz, 2016), some account for secondary porosity (Morin and Michel, 2018), and non-axisymmetric void shapes (Barrioz et al., 2019). These developments have enabled predictions of Lode effects in ductile failure (Torki et al., 2021), including under shear (Torki and Benzerga, 2018) or plane stress loading (Torki and Benzerga, 2022), which were heretofore only possible using *ad hoc* criteria.

A common feature of the effective yield criteria developed by Benzerga and Leblond (2014) and subsequent efforts, as well as those developed earlier using different approaches, e.g. Pardoen and Hutchinson (2000), Benzerga (2002) and Tekoğlu et al. (2012), is that they are limited to void coalescence in planar bands, Fig. 1a,b. This is arguably the most common, most deleterious microscopic void linkup mechanism. It is, however, insufficient to fully describe the range of potential behaviors of a porous material. Gologanu et al. (1994a) carried out axisymmetric voided cell calculations similar to those by Koplik and Needleman (1988) but

^{*} Correspondence to: Texas A&M University, Aerospace Engineering, MS 3141 College Station, TX 77843, USA. E-mail address: benzerga@tamu.edu (A.A. Benzerga).

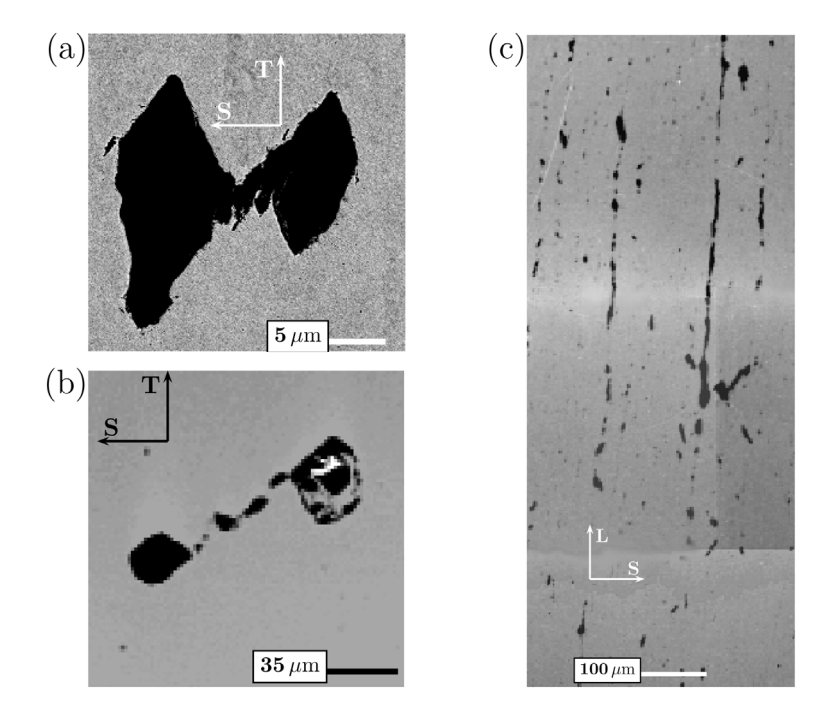


Fig. 1. Coalescence by internal (a) necking or (b) shearing; (c) Necklace coalescence. Source: After Benzerga (2000).

considering stress states with a major radial stress. In terms of recent literature, their calculations considered both cases of the Lode parameter L = -1 (generalized tension) and L = 1 (generalized compression). The reader is referred to Benzerga and Leblond (2010) for specific definitions. Under generalized tension, void coalescence was found to occur in layers as in Koplik and Needleman (1988) but under generalized compression, void coalescence was found to occur in columns. This phenomenon, first discovered numerically by Gologanu et al. (1994a), was subsequently observed in steel bars by Benzerga (2000), albeit for initially non-spherical voids, Fig. 1c.

The phenomenon of void coalescence in columns, or as termed in Benzerga (2000) "necklace coalescence", may be described as follows. When a porous material is subjected to some macroscopic deformation, the porosity attributes (volume, shape, spacing) evolve until strains eventually concentrate in plugs that axially connect the voids in their current state, Fig. 2a. The plugs thus make up columns of ruined material in the sense of limit load analysis. In contrast with coalescence in layers, Fig. 2b, void coalescence in columns has a subtle effect on the effective response in an actual evolution problem. This is so because a ruined planar band is more damaging than a ruined cylinder. In particular, the phenomenon does not seem to be accompanied by partial elastic unloading within the cell. This implies a subtle signature of the event on the overall response.

Conditions under which plastic collapse would occur in plugs and not in layers can only be determined if both mechanisms are first analyzed separately. There is indication from previous work (Gologanu et al., 1994a) that for initially spherical voids a clear distinction between the two regimes is possible via the overall stress state, more precisely the Lode parameter. However, as discussed by Benzerga (2000) coalescence in columns is observed (hence possible) under generalized tension for sufficiently elongated voids.

Gologanu and co-workers (Gologanu, 1997; Gologanu et al., 2001b) developed a criterion for void coalescence in columns. They considered a porous cylindrical cell modeled as a composite consisting of a fully dense torus surrounding a porous central cylinder. Plastic flow was modeled using J_2 flow theory in the torus and an effective porous plasticity model (Gologanu et al., 1997) in the central cylinder. In this two-step homogenization process, the effect of discrete voids is smeared out and the predictive capability of the final criterion hinges on that of the model assumed inside the porous region. From a methodology point of view, this criterion is similar to the model of void coalescence in layers of Gologanu et al. (2001a). However, recent progress in micromechanical modeling of void coalescence opens up the possibility to revisit the same problem from first principles of limit analysis combined with results from homogenization theory following the general principles outlined, for example, in Benzerga and Leblond (2010). This is precisely the task undertaken in the present paper. In a sense, the criterion to be sought stands for that of Gologanu et al.'s (2001b) just as the criterion of coalescence in layers developed by Benzerga and Leblond (2014) stands for an earlier criterion by Gologanu et al. (2001a).

The paper is organized as follows. Section 2 contains the whole analytical treatment with derivation details deferred to appendices. Section 3 presents two assessment methods. The first uses putatively exact results and relies on finite-element based limit analysis (Section 3.1). The second makes reference to a previous analytical yield criterion that accounts for void growth and coalescence in layers (Section 3.2). All results are presented and discussed in context in Section 4.

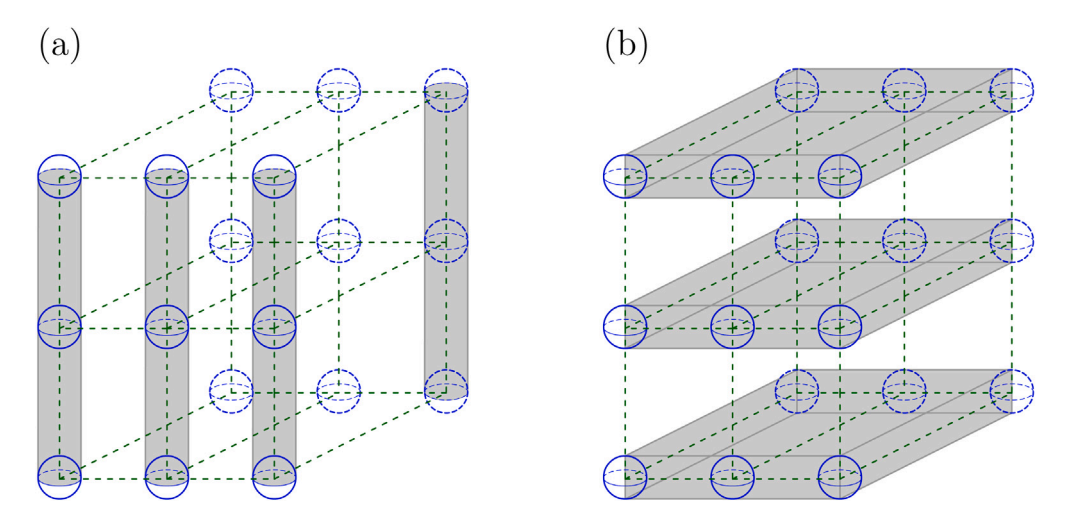


Fig. 2. Idealization of the mechanisms in Fig. 1 for a periodic aggregate of voids. (a) Coalescence in columns. (b) Coalescence in layers.

2. Analytical approach

2.1. Problem statement

The effective yield criterion of a porous material is determined using the following variational principle; see e.g. (Benzerga and Leblond, 2010; Torki et al., 2015):

$$\forall \mathbf{D}, \quad \mathbf{\Sigma} : \mathbf{D} \le H(\mathbf{D}), \qquad H(\mathbf{D}) = \inf_{\mathbf{v} \in \mathcal{K}(\mathbf{D})} \left[\langle \sup_{\sigma^* \in C} \sigma^*_{ij} d_{ij} \rangle_{\Omega} + \frac{1}{\Omega} \int_{S} \sup_{\sigma^* \in C} t^*_{i} \llbracket v_{i} \rrbracket \, \mathrm{d}S \right]$$
(1)

Here, Σ and \mathbf{D} are volume averages of the microscopic Cauchy stress σ and rate of deformation \mathbf{d} , respectively, and $\Pi(\mathbf{D})$ is the effective plastic dissipation. Also, $\mathcal{K}(\mathbf{D})$ denotes the set of kinematically admissible and incompressible velocity fields \mathbf{v} associated with \mathbf{D} , C is the convex of reversibility, and $\langle \cdot \rangle_{\Omega}$ stands for averaging over domain Ω (identified with its volume). The writing in Eq. (1) accounts for the possibility of there being a surface S across which the (tangential) velocity field is discontinuous. In such cases, $[\![\mathbf{v}]\!]$ is the velocity jump and \mathbf{t}^* is the surface traction. If the dissipation function is differentiable then the effective yield surface is parametrically given by:

$$\Sigma = \frac{\partial \Pi}{\partial \mathbf{D}} \tag{2}$$

In computational formulations of this problem, using either special or standard finite elements, e.g. Trillat and Pastor (2005) and Madou and Leblond (2012), the admissible velocity fields emerge as part of the solution to the minimization in Eq. (1). The exact velocity fields (which are continuous) may be diffuse or localized in the matrix. Following a recently introduced terminology (Torki and Benzerga, 2018), diffuse velocity fields correspond to homogeneous yielding of the porous material whereas localized velocity fields are associated with inhomogeneous yielding. The regime of void coalescence, whether in layers or columns, always corresponds to a mode of inhomogeneous yielding. One important consequence of inhomogeneous yielding is that the boundary conditions on the velocity fields cannot be of the uniform strain rate type.

In seeking an analytical model of void coalescence in columns, velocity fields are posited and an estimate of the effective dissipation is derived. The chosen velocity fields must therefore be consistent with an appropriate mode of inhomogeneous yielding, as sketched in Fig. 2a. Using trial velocity fields potentially leads to an upper bound estimate of the effective yield domain, as discussed in Benzerga and Leblond (2010). Developing the new model thus involves choosing: (i) a suitable elementary cell Ω ; (ii) a plastic flow model in the matrix; and (iii) trial velocity fields consistent with the phenomenon of coalescence in columns.

2.2. Elementary cell

Consider an elementary cylindrical cell embedding a coaxial cylindrical void and acted upon by macroscopic axial and lateral stresses as outlined in Fig. 3a. The loading is assumed to be axially symmetric. Consideration of arbitrary stress states or void distributions is beyond the scope of the first analysis presented here. In anticipation of the possibility of void coalescence in columns, the cell is divided in three subparts: the void (V), the matrix (M) exclusive of plugs, and the plugs (P). The overall domain of the cell, identified with its volume Ω , is thus written as:

$$\Omega = \Omega^{(P)} + \Omega^{(V)} + \Omega^{(M)} \tag{3}$$

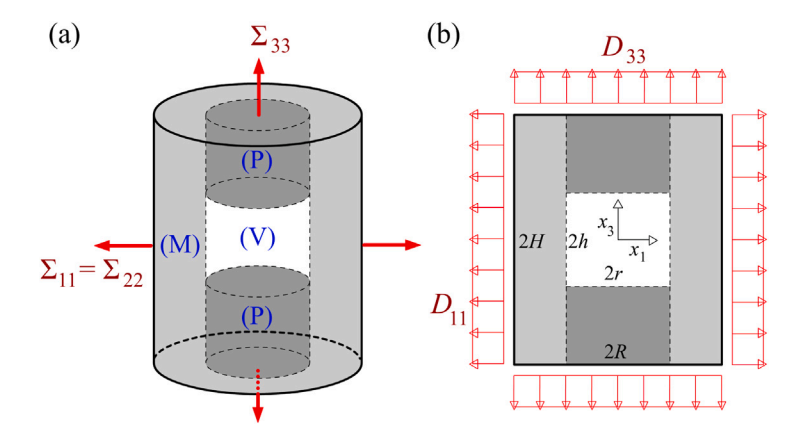


Fig. 3. (a) Cylindrical cell representing column coalescence under triaxial loading. (b) Meridian section of the cell, also showing the overall rate-of-deformation.

If r and h denote the void's radius and height, respectively, and R and H the cell's radius and height (Fig. 3b) and if ω is the void volume then the following definitions apply:

$$f = \frac{\omega}{\Omega}, \quad \chi = \frac{r}{R}, \quad w = \frac{h}{r}, \quad \lambda = \frac{H}{R}, \quad c = \frac{h}{H} = \frac{\chi w}{\lambda}$$
 (4)

Here, f is the void volume fraction, χ the transverse ligament parameter, w the void aspect ratio, λ the cell aspect ratio, and c the axial ligament parameter. Only three of the above five parameters are independent. For instance, $f = c\chi^2 = \chi^3 w/\lambda$ for the considered geometry.

The elementary cell of Fig. 3a is not space filling, but is meant to approximate the situation depicted in Fig. 2a or a circumscribing hexagonal-prismatic cell, as often considered in the literature (Tvergaard, 1982). Furthermore, cylindrical cells have been used in all previous analyses of void coalescence in layers (Benzerga and Leblond, 2014; Torki et al., 2015, 2017; Morin et al., 2015; Keralavarma and Chockalingam, 2016; Barrioz et al., 2019).

2.3. Kinematic constraints

Coalescence in columns is accompanied with a *finite* strain concentration in the plugs. Plastic flow continues in both (M) and (P) regions but with different rates. With this in mind, one can relate the average rates of deformation in the matrix and porous regions to their overall counterparts.

First, overall strain compatibility entails that the following relationships hold among the axial rates of deformation:

$$D_{33}^{(P+V)} = D_{33}^{(M)} = D_{33}$$
 (5)

where superscript (P + V) refers to the central region that contains the void, and the notation $\mathbf{D}^{(X)}$ stands for $(\int_{\Omega^{(X)}} \mathbf{d} \, \mathrm{d}\Omega)/\Omega^{(X)}$. The rate of deformation in the matrix being traceless $(d_{kk}^{(M)} = 0)$ one can write:

$$D_{kk} = \frac{1}{\Omega} \int_{\Omega} d_{kk} \, \mathrm{d}\Omega = \frac{1}{\Omega} \int_{\Omega^{(\mathrm{P+V})}} d_{kk}^{(\mathrm{P+V})} \, \mathrm{d}\Omega = \frac{\chi^2}{\Omega^{(\mathrm{P+V})}} \int_{\Omega^{(\mathrm{P+V})}} d_{kk}^{(\mathrm{P+V})} \, \mathrm{d}\Omega = \chi^2 D_{kk}^{(\mathrm{P+V})}$$
 (6)

Hence, combining this result with Eq. (5), one obtains the transverse strain rate in the porous region as:

$$D_{11}^{(P+V)} = \frac{D_{11}}{\chi^2} + \frac{1}{2} \left(\frac{1}{\chi^2} - 1 \right) D_{33} \tag{7}$$

Finally, exploiting again the isochoric nature of plastic flow in the matrix, the condition $D_{kk}^{(M)} = 0$ implies, with due account of Eq. (5):

$$D_{11}^{(M)} = -\frac{1}{2}D_{33} \tag{8}$$

Thus, merely considering strain concentration in plugs delivers kinematic constraints on the average strain rates in the porous and matrix regions. The ensuing constraints, Eqs. (5), (7) and (8), are valid irrespective of whether the void is treated discretely (this paper) or smeared out, as in Gologanu et al. (2001b).

2.4. Trial velocity fields

To accommodate inhomogeneous yielding, the trial velocity fields must be localized. In the matrix, a Gurson-like velocity field, $\mathbf{v}^{(M)}$, is given in cylindrical coordinates (ρ, θ, z) :

$$v_{\rho}^{(M)} = \frac{R}{2} \left[D_{kk} \frac{R}{\rho} - D_{33} \frac{\rho}{R} \right], \qquad v_{z}^{(M)} = D_{33} z \tag{9}$$

which satisfy boundary conditions $v_z^{(M)}(H) = D_{33}H$ and $v_a^{(M)}(R) = D_{11}R$.

In the plugs, two velocity fields are alternatively used. The simplest is a "parallel" (z-independent) field whereby the radial component takes the form:

$$v_{\nu}^{(\mathbf{p})}(\rho) = A\rho$$
 (10)

and the axial component is obtained from the incompressibility condition:

$$\operatorname{div} \mathbf{v}^{(P)} \equiv v_{\rho,\rho}^{(P)} + \frac{v_{\rho}^{(P)}}{\rho} + v_{z,z}^{(P)} = 0 \quad \Rightarrow \quad v_{z}^{(P)} = -2Az + B(\rho)$$
(11)

A simple choice that will be shown later to deliver a closed-form solution consists of taking $B(\rho)$ as a constant, say B. Parameters A and B are then fully determined from boundary (and continuity) conditions, namely $v_{\rho}^{(P)}(r) = v_{\rho}^{(M)}(r) \Rightarrow A = D_{11}^{(P+V)}$, on account of Eq. (7), and $v_{z}^{(P)}(H) = D_{33}H \Rightarrow B = D_{kk}^{(P+V)}H$, so that:

$$\begin{cases} v_{\rho}^{(P)} = \frac{1}{2} \left(\frac{D_{kk}}{\chi^2} - D_{33} \right) \rho \\ v_z^{(P)} = \frac{D_{kk}}{\chi^2} (H - z) + D_{33} z \end{cases}$$
 (12)

where Eqs. (5) and (7) have been used. Note that the first component may be written as: $v_{\rho}^{(P)} = D_{11}^{(P+V)} \rho$. A shortcoming of the field given by Eq. (12) is that it is discontinuous across the P–M interface with the jump in the tangential component v_{τ} given by:

$$[[v_z(z)]]_{\rho=r} = \frac{D_{kk}}{\gamma^2} (H - z) \tag{13}$$

A more realistic velocity field in the plugs is constructed by requiring that the axial component be continuous across the P-M interface. This may be accomplished by including some radial dependence of $v_c^{(p)}$ in the first term in Eq. (12), then obtaining the radial component from the incompressibility constraint. Thus, the second trial field is given by:

$$\begin{cases} v_{\rho}^{(p)} = -\frac{\rho}{2} \left\{ D_{33} + \frac{D_{kk}}{\chi^2} \left[-2 + \left(\frac{\rho}{r} \right)^2 \right] \right\} \\ v_{z}^{(p)} = 2 \left[1 - \left(\frac{\rho}{r} \right)^2 \right] \frac{D_{kk}}{\chi^2} (H - z) + D_{33} z \end{cases}$$
(14)

and satisfies all kinematic constraints.

Fig. 4 illustrates both velocity fields superposed onto contours of the equivalent strain rate d_{eq} for various combinations of D_{11} and D_{33} . Note that $D_{kk} = 0$ in Fig. 4a such that the discontinuous field becomes continuous and indistinguishable from that shown

2.5. Effective dissipation

Having so chosen the trial velocity fields, the corresponding plastic dissipation is necessarily larger than the infimum given by Eq. (1)₂ and the yield criterion defined parametrically through the inequality in Eq. (1)₁ is an upper bound to the actual one. In what follows, we shall still denote by $\Pi(\mathbf{D})$ the dissipation evaluated for the above trial fields.

To analyze potential collapse mechanisms, the material is modeled as rigid-ideally plastic and obeying J_2 flow theory (von Mises criterion with an associated flow rule). The volumetric term in Eq. (1)2 is then expressed as:

$$\Pi^{\text{vol}} = \frac{1}{\Omega} \int_{\Omega \setminus \Omega^{(V)}} \bar{\sigma} d_{\text{eq}} \, d\Omega, \qquad d_{\text{eq}} = \sqrt{\frac{2}{3} \mathbf{d} : \mathbf{d}}$$
(15)

where $\bar{\sigma}$ is the tensile yield strength and $d_{\rm eq}$, the von Mises equivalent strain rate, is associated with one of the two trial velocity fields introduced above. The integral in Eq. (15) is divided into the matrix and plug domains as follows:

$$\Pi^{\text{vol}} = \frac{1}{\Omega} \int_{\Omega^{(M)}} \bar{\sigma} d_{\text{eq}}^{(M)} d\Omega + \frac{1}{\Omega} \int_{\Omega^{(P)}} \bar{\sigma} d_{\text{eq}}^{(P)} d\Omega \tag{16}$$

where $d_{eq}^{(M)}$ and $d_{eq}^{(P)}$ are the equivalent strain rates, defined as in Eq. (15)₂, but associated with the matrix and plug velocity fields, respectively. The first integral in Eq. (16) is the same for both sets of velocity fields introduced in Section 2.4. Using Eq. (9) one

$$d_{\rho\rho}^{(M)} = v_{\rho,\rho}^{(M)} = -\frac{1}{2} \left(D_{kk} \frac{R^2}{\rho^2} + D_{33} \right)$$

$$d_{\theta\theta}^{(M)} = \frac{v_{\rho}^{(M)}}{\rho} = \frac{1}{2} \left(D_{kk} \frac{R^2}{\rho^2} - D_{33} \right)$$

$$d_{zz}^{(M)} = v_{z,z}^{(M)} = D_{33}$$

$$(17)$$

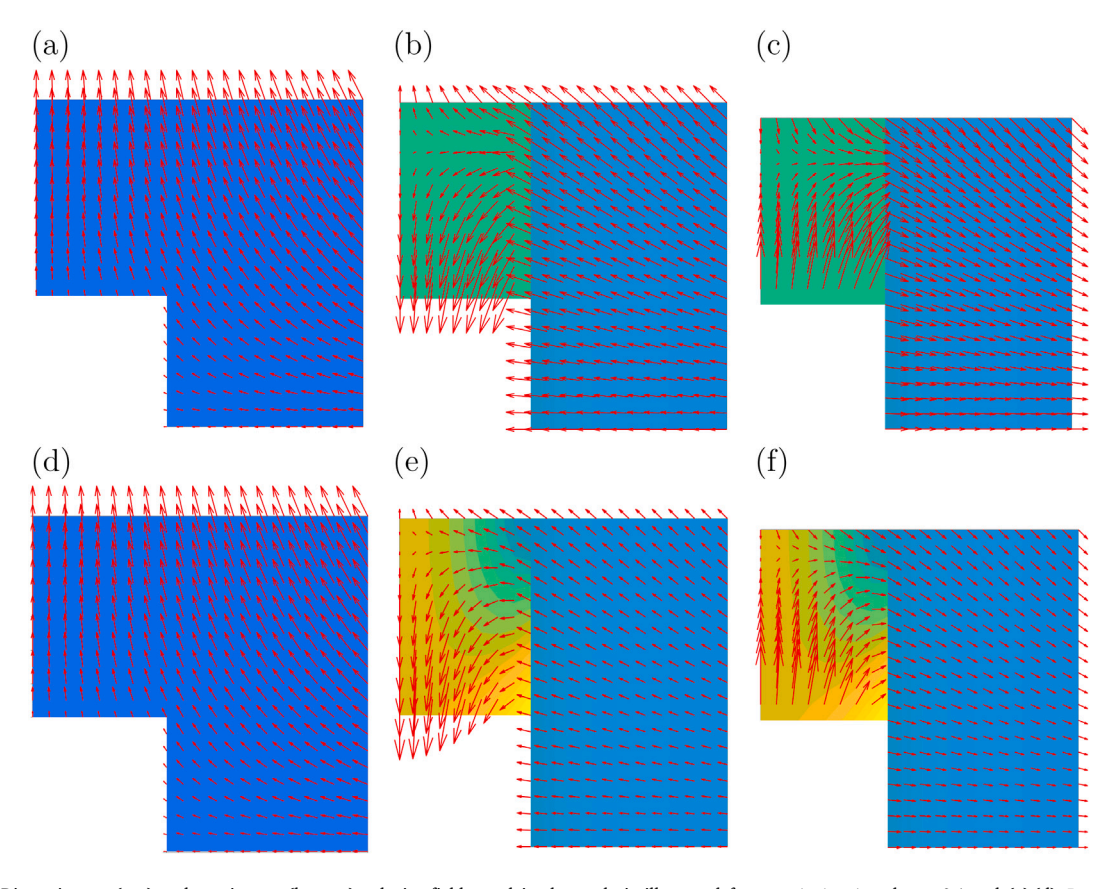


Fig. 4. Discontinuous (top) and continuous (bottom) velocity fields used in the analysis illustrated for w=1, $\lambda=1$ and $\chi=0.4$ and (a),(d) $D_{11}=-0.5D_{33}$, $D_{33}>0$; (b),(e) $D_{11}=-D_{33}$, $D_{33}>0$; (c),(f) $D_{11}=-D_{33}$, $D_{33}<0$. Contours of d_{eq} are also shown in arbitrary units.

Hence,

$$d_{\rm eq}^{\rm (M)} = \sqrt{\frac{1}{3}D_{kk}^2 \frac{R^4}{\rho^4} + D_{33}^2}$$
 (18)

Using the change of variable $(\rho, z) \to (U, v)$ with $U = (\rho/R)^2$ and v = z/H, and introducing the ratio

$$\xi = \frac{D_{kk}}{\sqrt{3}D_{33}},\tag{19}$$

the first integral in Eq. (16), denoted $\Pi^{(M)}$, is written as:

$$\Pi^{(M)} = \int_{v=0}^{v=1} \int_{U=\chi^2}^{U=1} \bar{\sigma} d_{\text{eq}}^{(M)}(U) \, dU \, dv = \bar{\sigma} \int_{\chi^2}^{1} d_{\text{eq}}^{(M)}(U) \, dU = \bar{\sigma} |D_{33}| \int_{\chi^2}^{1} \sqrt{\left(\frac{\xi}{U}\right)^2 + 1} \, dU$$
 (20)

where the integrand only depends on U since the Gurson-like velocity field used in the matrix is linear in z. Upon integration one gets:

$$\Pi^{(M)} = \bar{\sigma} \frac{|D_{kk}|}{\sqrt{3}} \left[\sqrt{1 + \left(\frac{U}{\xi}\right)^2} - \sinh^{-1}\left(\frac{\xi}{U}\right) \right]_{U=\chi^2}^1$$
(21)

The function $\Pi^{(M)}(\mathbf{D})$ is differentiable. This is evident from the definition of $d_{\mathrm{eq}}^{(M)}$ in Eq. (18).

2.5.1. Discontinuous field

The second integral in Eq. (16) depends on the choice made for the velocity fields in the plugs. The field given by Eq. (12) ensures *minimum continuity* in that the tangential component is discontinuous across the matrix–plug interface while field Eq. (14) is *fully continuous*.

With reference to Eq. (12), the components of $\mathbf{d}^{(P)}$ are given by:

$$d_{qq}^{(P)} = d_{\theta\theta}^{(P)} = D_{11}^{(P+V)}, \qquad d_{77}^{(P)} = -2D_{11}^{(P+V)}$$
(22)

where $D_{11}^{(P+V)}$ is given by Eq. (7). Hence,

$$d_{\text{eq}}^{(P)} = 2 \left| D_{11}^{(P+V)} \right| \tag{23}$$

The corresponding contribution to Π^{vol} then reads:

$$\Pi^{(P)} = \frac{1}{\Omega} \int_{\Omega^{(P)}} \bar{\sigma} d_{\text{eq}}^{(P)} d\Omega = 2 \frac{\Omega^{(P)}}{\Omega} \bar{\sigma} \left| D_{11}^{(P+V)} \right| = 2(1 - c) \chi^2 \bar{\sigma} \left| D_{11}^{(P+V)} \right|$$
(24)

which is expressed in final form as:

$$\Pi^{(P)} = (1 - c)\bar{\sigma}|D_{kk} - \chi^2 D_{33}| \tag{25}$$

Finally, the surface term in Eq. $(1)_2$ writes:

$$\Pi^{\text{surf}} = \frac{1}{\Omega} \int_{S_{\text{int}}} \bar{\tau} [v_z] dS \tag{26}$$

Here, $\bar{\tau} = \bar{\sigma}/\sqrt{3}$ is the shear yield strength, $S_{\rm int}$ is the P–M interface connecting (P) and (M) regions at $\rho = r$ (see Fig. 3a) and $[v_z]$ is the velocity jump, given by Eq. (13), across that interface. Therefore, on account of there being two plugs

$$\Pi^{\text{surf}} = \frac{\bar{\tau}}{\pi R^2 H} \int_0^{2\pi} \int_h^H \frac{|D_{kk}|}{\chi^2} (H - z) r \, \mathrm{d}\theta \, \mathrm{d}z \tag{27}$$

which, upon simplification, evaluates to:

$$\Pi^{\text{surf}} = \frac{w}{c} (1 - c)^2 \bar{\tau} |D_{kk}| \tag{28}$$

where w and c are defined in Eq. (4).

To sum up, for the discontinuous field defined by Eq. (9) in the matrix and Eq. (12) in the plugs, the total dissipation is written as:

$$\Pi = \Pi^{(M)} + \Pi^{(P)} + \Pi^{\text{surf}}$$
(29)

with $\Pi^{(M)}$ given by Eq. (21), $\Pi^{(P)}$ by Eq. (25), and Π^{surf} by Eq. (28). The dissipation function given by Eq. (29) is non-differentiable owing to the presence of absolute values in the expressions Eq. (25) and Eq. (28) of $\Pi^{(P)}$ and Π^{surf} . In Eq. (28) non-differentiability is due to the surface term. On the other hand, in Eq. (25) it is due to the uniformity of the rate of deformation in the plugs.

2.5.2. Continuous field

If now the velocity field of Eq. (14) is used in the plugs, the components of $\mathbf{d}^{(P)}$ (not given for brevity) yield the following expression for $d_{\text{eq}}^{(P)}$ in terms of $u = (\rho/r)^2$, v = z/H as above, and the ratio ξ in Eq. (19):

$$d_{\rm eq}^{\rm (P)} = \sqrt{\mathcal{R}(u,v)} |D_{33}| \tag{30}$$

where

$$\mathcal{R}(u,v) = \mathcal{V}_0 + 2\mathcal{V}_1(v)u + \mathcal{V}_2 u^2 \tag{31}$$

and

$$\mathcal{U}_{0} = (\bar{\xi} - 1)^{2}
\mathcal{U}_{1} = \bar{\xi} + \bar{\xi}^{2} (\delta(v) - 1)
\mathcal{U}_{2} = \frac{13}{12} \bar{\xi}^{2}$$
(32)

Here,

$$\bar{\xi} = 2\sqrt{3} \frac{\xi}{\chi^2}$$

$$\delta(v) = \frac{2}{3} \left(\frac{w(1-v)}{c} \right)^2$$
(33)

Note that all dependence upon v enters through the function $\delta(v)$.

In this case, the second integral in Eq. (16) reduces to:

$$H^{(P)} = \bar{\sigma} |D_{33}| \chi^2 \int_c^1 \int_0^1 \sqrt{\mathcal{R}(u, v)} \, \mathrm{d}u \, \mathrm{d}v$$
 (34)

Consider first the trivial case of $D_{kk}=0$, for which $\bar{\xi}=0$, hence $\mathcal{U}_0=1$ and $\mathcal{U}_1=\mathcal{U}_2=0$. Therefore, $\mathcal{R}(u,v)=1$ and $\Pi^{(P)}=(1-c)\chi^2\bar{\sigma}|D_{33}|$. More generally, if $D_{kk}\neq 0$, $\Pi^{(P)}$ can be integrated in u, but the obtained result cannot be analytically integrated in v. Adopt the notation:

$$I(v) = \int_0^1 \sqrt{R(u,v)} \, \mathrm{d}u \tag{35}$$

and introduce the following discriminant (conveniently taken as the negative of the usual discriminant of a second-degree polynomial) in relation to Eq. (31):

$$\Delta(v) = V_0 V_2 - V_1^2 \tag{36}$$

where it should be noted that U_1 depends on v. The case $\Delta < 0$ is covered in Appendix B as it is rare. Then, so long as $\Delta \ge 0$ the integral \mathcal{I} may be expressed as (see Gradshtein and Ryzhik (1971))

$$I(v) = \frac{1}{2} \left[(u + B(v)) \sqrt{\mathcal{R}(u, v)} + \mathcal{P}(v) \ln |\mathcal{L}(u, v)| \right]_{u=0}^{1}$$
(37)

since $U_2 > 0$. Here,

$$\mathcal{B} = \frac{\mathcal{U}_{1}}{\mathcal{U}_{2}} = \frac{12}{13} \left(\frac{1}{\bar{\xi}} + \delta - 1 \right)$$

$$\mathcal{P} = \frac{\mathcal{U}_{0} - \frac{\mathcal{U}_{1}^{2}}{\mathcal{U}_{2}}}{\sqrt{\mathcal{U}_{2}}} = \sqrt{\frac{12}{13}} \frac{1}{|\bar{\xi}|} \left[(\bar{\xi} - 1)^{2} - \frac{12}{13} \left(1 + \bar{\xi}(\delta - 1) \right)^{2} \right]$$

$$\mathcal{L} = \sqrt{\mathcal{U}_{2} \mathcal{R}(u, v)} + \mathcal{U}_{2} u + \mathcal{U}_{1}$$
(38)

The fact that $\lim_{\xi \to 0} I(v) = 1$ for all v may not be evident from the above equations, but the property results directly from the very definition of the dissipation function and can be verified.

To sum up, for the continuous field defined by Eq. (9) in the matrix and Eq. (14) in the plugs, the total dissipation reads

$$\Pi = \Pi^{(M)} + \Pi^{(P)} \tag{39}$$

with $\Pi^{(M)}$ given by Eq. (21), $\Pi^{(P)}$ by Eq. (34). The dissipation function given by Eq. (39) is differentiable.

2.6. Yield criterion

From what precedes it follows that two representations are possible for the yield criterion of a porous material in the regime of coalescence in columns. The advantage of using the less realistic discontinuous velocity field {Eqs. (9), (12)} is that closed-form solutions are possible *a priori*. However, because the dissipation function is not differentiable, derivations must proceed from the fundamental inequality (1) of limit analysis. Hence, they are tedious. The reader is referred to Appendix A for all corresponding derivations. On the other hand, one advantage of using the continuous field {Eqs. (9), (14)} is that the derivation of the yield criterion is more straightforward as it proceeds from the parametric form of Eq. (2). However, a closed-form solution is not possible because the dissipation itself is not available in closed form.

2.6.1. Exact form using discontinuous field

The yield criterion based on the discontinuous velocity field $\{\text{Eqs. (9), (12)}\}\$ and corresponding dissipation, Eq. (29), is defined by (the order in which the + and - signs are given matters):

$$\Sigma_{33} - \Sigma_{11} = \pm \bar{\sigma}(1 - c\chi^2) \quad \text{for} \quad \left| \frac{\Sigma_{11}}{\bar{\sigma}} \pm (1 - c) \right| \le \frac{w}{\sqrt{3}} \frac{(1 - c)^2}{c}$$

$$(\Sigma_{33} - \Sigma_{11}) + \chi^2 \Sigma_{11} = \pm A \quad \text{for} \quad \left| \frac{\Sigma_{11}}{\bar{\sigma}} \mp \frac{B}{\sqrt{3}} \right| \le 1 - c$$

$$\left[\frac{\Sigma_{33} - \Sigma_{11}}{\bar{\sigma}} + \epsilon_1 (1 - c) \chi^2 \right]^2 + 2\chi^2 \cosh \left[\sqrt{3} \frac{\Sigma_{11}}{\bar{\sigma}} - \epsilon_1 \sqrt{3} (1 - c) - \epsilon_2 w \frac{(1 - c)^2}{c} \right] - 1 - \chi^4 = 0 \quad \text{otherwise}$$

where A and B in Eq. $(40)_2$ are functions of the internal parameters given by:

$$\frac{\sqrt{3}}{\bar{\sigma}}A = \sqrt{\chi^4 + 3} + \chi^2 \left(\sinh^{-1}\frac{1}{\sqrt{3}} - 2\right) - \chi^2 \sinh^{-1}\frac{\chi^2}{\sqrt{3}} + \chi^2 w \frac{(1 - c)^2}{c}$$

$$B = \sinh^{-1}\frac{1}{\sqrt{3}} - \sinh^{-1}\left(\frac{\chi^2}{\sqrt{3}}\right) + w \frac{(1 - c)^2}{c}$$
(41)

and $\epsilon_1 = \operatorname{sgn}(D_{kk} - \chi^2 D_{33})$, $\epsilon_2 = \operatorname{sgn}(D_{kk})$. See Appendix A for derivation details.

2.6.2. Implicit form using continuous field

In this case, the yield surface is parametrically defined using Eq. (2) where the dissipation was calculated in Section 2.5.2. Using Eq. (39) one can formally write:

$$\Sigma = \Sigma^{(M)} + \Sigma^{(P)}$$
 with $\Sigma^{(M)} = \frac{\partial \Pi^{(M)}}{\partial \mathbf{D}}$ and $\Sigma^{(P)} = \frac{\partial \Pi^{(P)}}{\partial \mathbf{D}}$ (42)

where $\Pi^{(M)}$ is given by Eq. (21) and $\Pi^{(P)}$ by Eq. (34). As is well known, the dissipation $\Pi(\mathbf{D})$ is positively homogeneous of degree 1; hence its derivative with respect to \mathbf{D} is homogeneous of degree 0. Therefore, in Eq. (42) the stresses depend on the components of \mathbf{D} only through their ratios.

Taking the axial symmetry into account, the first term in Eq. (42)₁ is specified through:

$$\frac{\Sigma_{11}^{(M)}}{\bar{\sigma}} \operatorname{sgn}\left(D_{kk}\right) = \frac{1}{\sqrt{3}} \left(\sinh^{-1}|\xi| - \sinh^{-1}\frac{|\xi|}{\chi^2} \right) \\
\frac{\Sigma_{33}^{(M)} - \Sigma_{11}^{(M)}}{\bar{\sigma}} \operatorname{sgn}\left(D_{kk}\right) = \sqrt{1 + \xi^2} - \sqrt{\xi^2 + \chi^4} \tag{43}$$

where ξ is the strain rate ratio introduced in Eq. (19).

To obtain the second term in Eq. (42)₁, note that the integrand in Eq. (34), i.e. the function $\mathcal{I}(v)$ in Eq. (37), depends on **D** through the ratio $\tilde{\xi}$ as per Eqs. (31), (33) and (38). Thus,

$$\Sigma_{11}^{(P)} = \frac{1}{2} \frac{\partial \Pi^{(P)}}{\partial D_{11}} = \frac{1}{2} \bar{\sigma} |D_{33}| \chi^2 \int_c^1 \frac{2}{\chi^2} \frac{2}{D_{33}} \frac{\partial I}{\partial \bar{\xi}} dv
\Sigma_{33}^{(P)} = \frac{\partial \Pi^{(P)}}{\partial D_{33}} = \bar{\sigma} \text{sgn} (D_{33}) \chi^2 \int_c^1 I dv + \bar{\sigma} |D_{33}| \chi^2 \int_c^1 \frac{\partial I}{\partial \bar{\xi}} \frac{\partial \bar{\xi}}{\partial D_{33}} dv$$
(44)

where the factor 1/2 in the first equation accounts for the special axisymmetric loading considered throughout. Straight from Eq. (37) one gets:

$$\frac{\partial I}{\partial \bar{\xi}} = \frac{1}{2} \left[\mathcal{B}' \sqrt{\mathcal{R}} + (u + \mathcal{B}) \mathcal{R}^* + \mathcal{P}' \ln |\mathcal{L}| + \mathcal{P} \frac{\mathcal{L}'}{\mathcal{L}} \right]_{u=0}^{1}$$
(45)

where, with reference to the definitions in Eq. (38) and $\bar{\xi}$ from Eq. (33):

$$B' = \frac{\partial B}{\partial \bar{\xi}} = \frac{-12}{13\bar{\xi}^2}$$

$$P' = \frac{\partial P}{\partial \bar{\xi}} = \frac{\sqrt{12}}{13^{3/2}} \operatorname{sgn}(\bar{\xi}) \left[-2(\delta - 1)^2 + 3 - \frac{1}{\bar{\xi}^2} \right]$$

$$R^* = \frac{1}{2\sqrt{R}} \frac{\partial R}{\partial \bar{\xi}} = \frac{\frac{13}{12} \bar{\xi} u^2 + [1 + 2(\delta - 1)\bar{\xi}] u + (\bar{\xi} - 1)}{\sqrt{\frac{13}{12} \bar{\xi}^2 u^2 + 2\bar{\xi}} [1 + (\delta - 1)\bar{\xi}] u + (\bar{\xi} - 1)^2}$$

$$\mathcal{L}' = \frac{\partial \mathcal{L}}{\partial \bar{\xi}} = \sqrt{\frac{13}{12}} |\bar{\xi}| R^* + \frac{13}{6} \bar{\xi} u + [1 + 2(\delta - 1)\bar{\xi}]$$

$$(46)$$

After simplifying and rearranging, one finally has:

$$\frac{\Sigma_{11}^{(P)}}{\bar{\sigma}}\operatorname{sgn}\left(D_{33}\right) = 2\int_{c}^{1} \frac{\partial \mathcal{I}}{\partial \bar{\xi}} dv$$

$$\frac{\Sigma_{33}^{(P)} - \Sigma_{11}^{(P)}}{\bar{\sigma}}\operatorname{sgn}\left(D_{33}\right) = \chi^{2}\int_{c}^{1} \mathcal{I} dv - \chi^{2}\bar{\xi}\int_{c}^{1} \frac{\partial \mathcal{I}}{\partial \bar{\xi}} dv$$
(47)

3. Assessment methodology

3.1. Numerical limit analysis

In order to assess the yield criteria derived in the previous section, numerical limit analysis in the sense of Madou and Leblond (2013) is used. The reader is referred to that paper for the basis of the finite element based procedure and its equivalence to classical limit analysis. Here, the procedure outlined by Torki et al. (2017) is specialized to axisymmetric loadings. Calculations have been carried out using the same unit cell considered in analytical modeling, Fig. 3. All calculations were carried out using ABAQUS (Version 6.14) with the option of geometric nonlinearity switched off. Madou and Leblond (2013) have shown that, under such circumstances, the discretized equations of the finite element problem are equivalent to those of limit analysis. The cell was discretized using eight-noded quadratic elements with reduced integration. Fig. 5 shows typical meshes used in the calculations.

A classical consequence of limit-analysis is that elastic strain rates vanish when the limit load is reached (Drucker et al., 1952; Leblond et al., 2018). Therefore, the elastic moduli disappear from the equations and may be chosen arbitrarily. Plastic flow then imposes an incompressible velocity field on the material. Here, in order to mimic such a velocity field, a high value of Poisson's

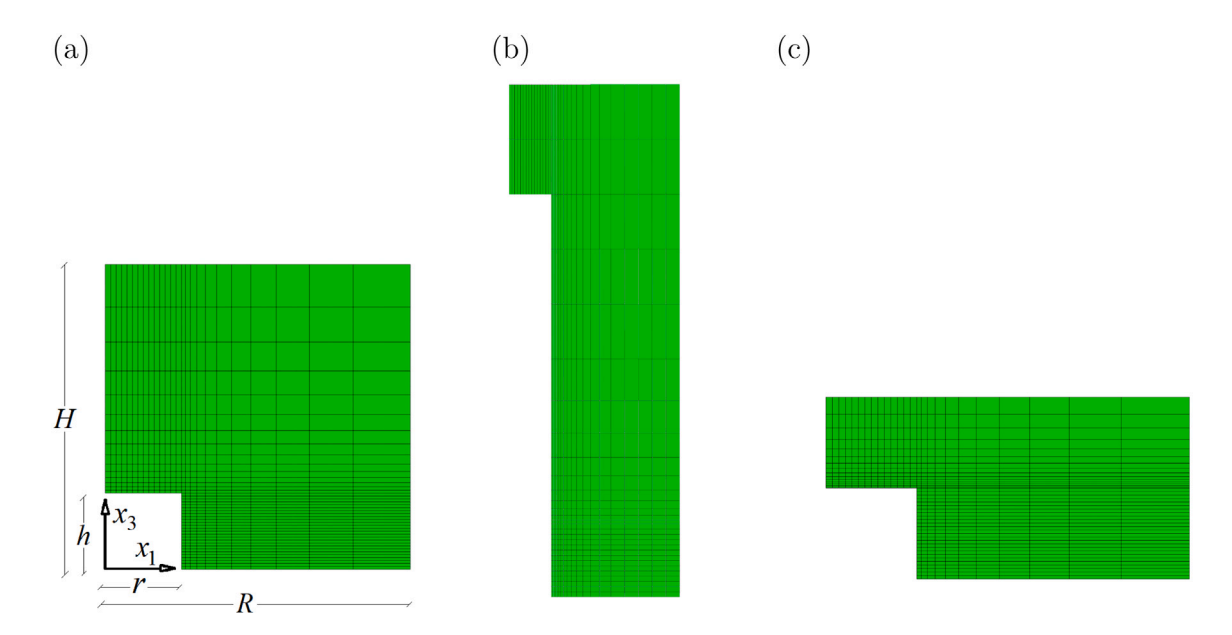


Fig. 5. Typical finite element meshes used in the calculations. (c) w = 1, $\lambda = 1$, $\chi = 0.25$. (b) w = 10, $\lambda = 3$, $\chi = 0.25$. (a) w = 1, $\lambda = 0.3$, $\chi = 0.25$.

ratio is enforced (v = 0.49). The material is then modeled as nearly elastically incompressible and ideally plastic. The yield strength to Young's modulus ratio is taken to be $\bar{\sigma}/E = 0.0002$.

One difficulty in using a cylindrical cell is that strictly periodic boundary conditions cannot be imposed. Instead, "quasi-periodic" boundary conditions are prescribed, as in Torki et al. (2017). In the absence of shear, these conditions amount to keeping the lateral boundaries straight. Using symmetry, half of the cell is meshed. With reference to Fig. 3, the macroscopic strain enforced on the cell is represented by the components

$$E_{11} = E_{22} \equiv \frac{R - R_0}{R_0} = \frac{U_1}{R_0}$$

$$E_{33} \equiv \frac{H - H_0}{H_0} = \frac{U_3}{H_0}$$
(48)

where U_1 denotes a prescribed displacement on the lateral surface and U_3 on the top surface. The imposed boundary conditions are thus: $u_3 = 0$ on the plane of symmetry $x_3 = 0$; $u_3 = E_{33}H$ on the top surface $x_3 = H$; and $u_r = E_{11}R$ on the lateral surface $\rho = R$.

The ratio between the lateral (Σ_{11}) and axial (Σ_{33}) stresses is governed by the U_1/U_3 ratio. Average stresses over the cell are calculated from a weighted summation over the average stresses in all elements; see Torki et al. (2017). The imposed displacements need to be large enough to ensure that the limit load is reached.

In previous work such as Torki et al. (2017) and Morin et al. (2015) it was common to impose $E_{11} = 0$ so as to focus on coalescence in layers. Here, no restriction is placed on E_{11} (hence on the U_1/U_3 ratio) so that either localized or non-localized behavior may emerge. In particular, the localized behavior can be of two types: either coalescence in layers or, as relevant here, coalescence in columns. On the other hand, a constraint must be exerted on the geometry to ensure that the cylindrical void does not protrude from the cell. The void fully fits into the cell provided that c < 1, where c is related to the (χ, w, λ) set by Eq. (4)₅.

3.2. Reference models

When comparison is made between the analytical model developed in Section 2 and numerical limit analysis, as described in the previous section, it is not uncommon that the yield surface corresponding to coalescence in columns lies very much exterior to the computed one. This is so because coalescence in columns only occurs for certain stress states and geometrical parameters. To complete the picture, it is therefore useful to introduce a hybrid yield surface that not only accounts for coalescence in columns but also for void growth and coalescence in layers. The latter two mechanisms are seamlessly accounted for in the unified model developed by Morin et al. (2016). These authors have used the same cylindrical geometry employed here, but with different mechanisms; see Fig. 6. Coalescence in layers corresponds to a uniaxial straining mode, Fig. 6b, whereas void growth corresponds to a triaxial straining mode, Fig. 6c.

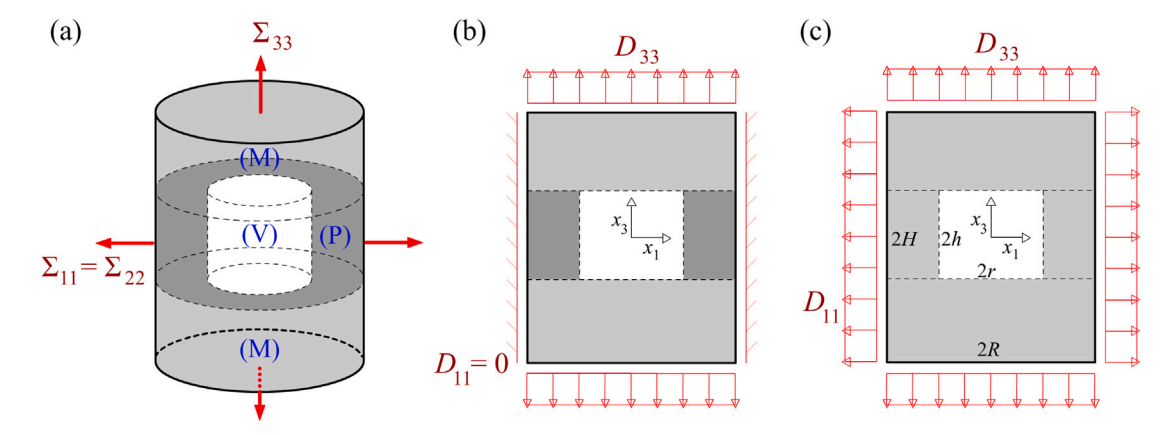


Fig. 6. (a) Cylindrical cell representing coalescence in layers. (b) Meridian section of the cell exhibiting the overall uniaxial straining mode. (c) Overall rate-of-deformation before strain localization.

The unified yield criterion of Morin et al. (2016) is defined by a piece-wise yield function, rewritten here following the formulation of Torki (2019):

$$\mathcal{F}^{\text{uni}} = \begin{cases} \mathcal{T} - (1 - \chi^{2}) & \text{if } |\mathcal{T}'| \leq \frac{t \Sigma^{\text{surf}}}{\bar{\sigma}} \\ \mathcal{T}^{2} + 2\chi^{2} \cosh \left[\sqrt{3} \left(\frac{\Sigma_{33} - \text{sgn} \left(D_{33} \right) t \Sigma^{\text{surf}}}{\bar{\sigma}} - \mathcal{T} \right) \right] - (1 + \chi^{4}) & \text{if } |\mathcal{T}| \geq \Gamma \end{cases}$$

$$\Gamma^{2} + 2\chi^{2} \cosh \left[\sqrt{3} \left(\frac{\Sigma_{33} - \text{sgn} \left(D_{33} \right) t \Sigma^{\text{surf}}}{\bar{\sigma}} - \Gamma \right) \right] - (1 + \chi^{4}) & \text{otherwise}$$

$$(49)$$

where

$$\begin{split} \mathcal{T} &= \frac{1}{c} \left[\frac{\Sigma_{33} - \Sigma_{11}}{\bar{\sigma}} + (1-c) \text{sgn} \left(-(1-c) + c \varGamma - \frac{\Sigma_{33} - \Sigma_{11}}{\bar{\sigma}} \right) \right] \\ \mathcal{T}' &= \frac{\Sigma_{11}}{\bar{\sigma}} + (1-c) \left[(1-\chi^2) + \text{sgn} \left(-(1-c) + c \varGamma - \frac{\Sigma_{33} - \Sigma_{11}}{\bar{\sigma}} \right) \right] \\ \varGamma^2(\chi) &= \frac{5}{2} + \chi^4 - \frac{4}{3} \sqrt{1 + 3\chi^4} \end{split}$$

Also,

$$\Sigma^{\text{surf}} = \frac{\bar{\sigma}}{3\sqrt{3}} \frac{\chi^3 - 3\chi + 2}{\chi w} \tag{50}$$

and

$$t(\chi, w) = \frac{(t_0 + t_1 \chi)w}{1 + (t_0 + t_1 \chi)w}$$
(51)

where t_0 and t_1 are parameters introduced by Torki et al. (2015) to improve the model in the case of penny-shaped cracks. The correction is relevant for w < 1.5.

Since Eqs. (40) and (49) are piecewise with overlapping intervals, one method to evaluate the effective (hybrid) surface is to calculate the radius of the yield locus in the Σ_{11} – Σ_{33} space for every value of Σ_{11} . The innermost surface will then be that corresponding to the minimum radius.

4. Results

Illustrations are given so as to (i) demonstrate the effect of trial velocity fields on yield surfaces corresponding to coalescence in columns (Section 4.1), (ii) compare with an earlier model by Gologanu et al. (2001b) (Section 4.2), (iii) investigate the competition with coalescence in layers (Section 4.3) and (iv) assess the new criterion against numerical limit analysis (Section 4.4).

4.1. Model variants

Fig. 7 schematically illustrates the effect of trial velocity field used in the limit analysis of coalescence in columns. The yield surface shown dashed corresponds to the criterion defined by Eq. (40) and obtained using the discontinuous velocity field {Eqs. (9) and (12)}. The yield surface shown solid corresponds to the criterion defined by {Eqs. (42), (43) and (47)} and obtained using the

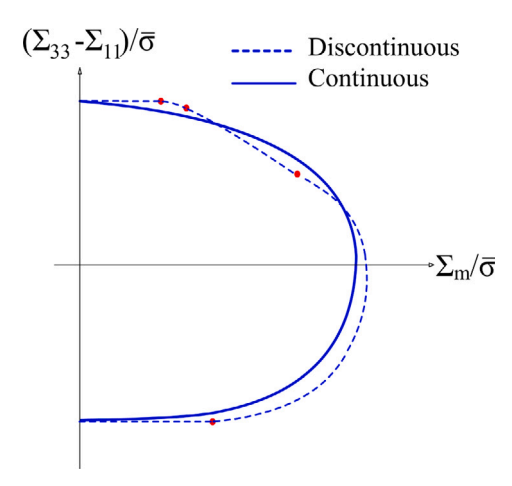


Fig. 7. Schematic comparison between typical yield loci accounting for void coalescence in columns based on discontinuous and continuous trial velocity fields.

continuous velocity field {Eqs. (9) and (14)}. Since no uncontrolled approximations were employed in deriving these two criteria, they each represent a rigorous upper bound to the true yield surface. The "discontinuous" yield surface contains singular flat parts and regular curved parts. Each part is defined by a closed-form expression; see Eq. (40). In Fig. 7 the various parts are separated by dots as a guide for the eye. The connection between the first regular part and the first singular part is cornerless. The junction between the two singular parts is also corner-free, as it is mediated by the second regular portion, which is small. On the other hand, the "continuous" yield surface is entirely smooth, as defined by parametric Eqs. (43) and (47). The regular surface can only be evaluated numerically because of integrals involving the function \mathcal{I} , not calculable analytically.

The discontinuity of velocity field {Eqs. (9) and (12)} is obviously non-physical. Yet, it is remarkable that the corresponding yield surface may produce a tighter upper-bound. This is noted wherever the dashed surface in Fig. 7 is interior to the solid one. A similar observation was made by Morin et al. (2015), in the context of coalescence in layers, for certain ranges of the internal parameters. Thus, discontinuous velocity fields cannot be disregarded on the sole basis of their being unphysical.

Fig. 8 shows actual yield surfaces predicted by both models for various values of the ligament parameter, χ , void aspect ratio, w, and cell aspect ratio, λ . All surfaces have point symmetry with respect to the origin, but the useful part for potential coalescence in columns is expected to lie in the lower-right quadrant ($\Sigma_{33} - \Sigma_{11} < 0$, $\Sigma_m > 0$).

At low hydrostatic stresses, the limit load is the least sensitive to the trial velocity field. This limit corresponds to minimal relative axial velocity between the plugs and the torus, with the cell admitting minimal, albeit nonzero, expansion. The difference between the two surfaces is also small for large values of χ and w or small values of λ . In all of these cases, the major contribution to the dissipation stems from the bulk (*i.e.* the torus or plugs) while the interfacial dissipation remains small.

On the other hand, at high levels of hydrostatic stress the "continuous" yield surface is most often exterior to the "discontinuous" surface. The discontinuous velocity field allows for sliding between the torus and the plugs, hence imposing less kinematic constraint and that leads, in this case, to a tighter upper bound. More generally, for small values of χ and w or large values of λ , the "discontinuous" surface clearly provides a better upper bound. A notable exception is the $\chi=0.4$ case in Fig. 8a.

In general, the "discontinuous" criterion stands closer to numerical values and will thus be favored over the "continuous" criterion for assessment purposes.

4.2. Comparison to Gologanu et al. (2001b)

An earlier criterion of void coalescence in columns was developed by Gologanu et al. (2001b) who used a two-step homogenization procedure (see Introduction). In it, the width of the central porous zone is set by a confocality condition between a spheroidal void and a spheroid that touches the top and bottom cell boundaries. The internal parameters entering their formulation are f, w and λ . Since voids are smeared out, the ligament parameter χ does not explicitly enter their model. Because their criterion and the present one differ in details of the elementary cell used, comparison is made at fixed void volume fraction f. Gologanu et al. (2001b) did not report any yield surfaces. However, Gologanu (1997) did for various values of f. The present model is thus evaluated using the relation $f = w\lambda/\chi^3$ (see Eq. (4) and text thereafter) and compared with the earlier model, Fig. 9. The surfaces of Gologanu et al. are replotted from Gologanu (1997). The reader may refer to Appendix C for a parametric formulation of their criterion. The results are presented for a rather small cell aspect ratio $\lambda = 1/3$, which favors coalescence in columns, as will be elaborated upon in Section 4.3.

For a relatively low porosity (f = 0.001) the surface predicted by the present model lies exterior to the surface predicted by the two-step homogenization criterion of Gologanu et al. (2001b), Fig. 9. As the porosity increases, the two surfaces intersect until eventually that predicted by the present model becomes interior to the earlier one; see for example the f = 0.1 surface in Fig. 9. This

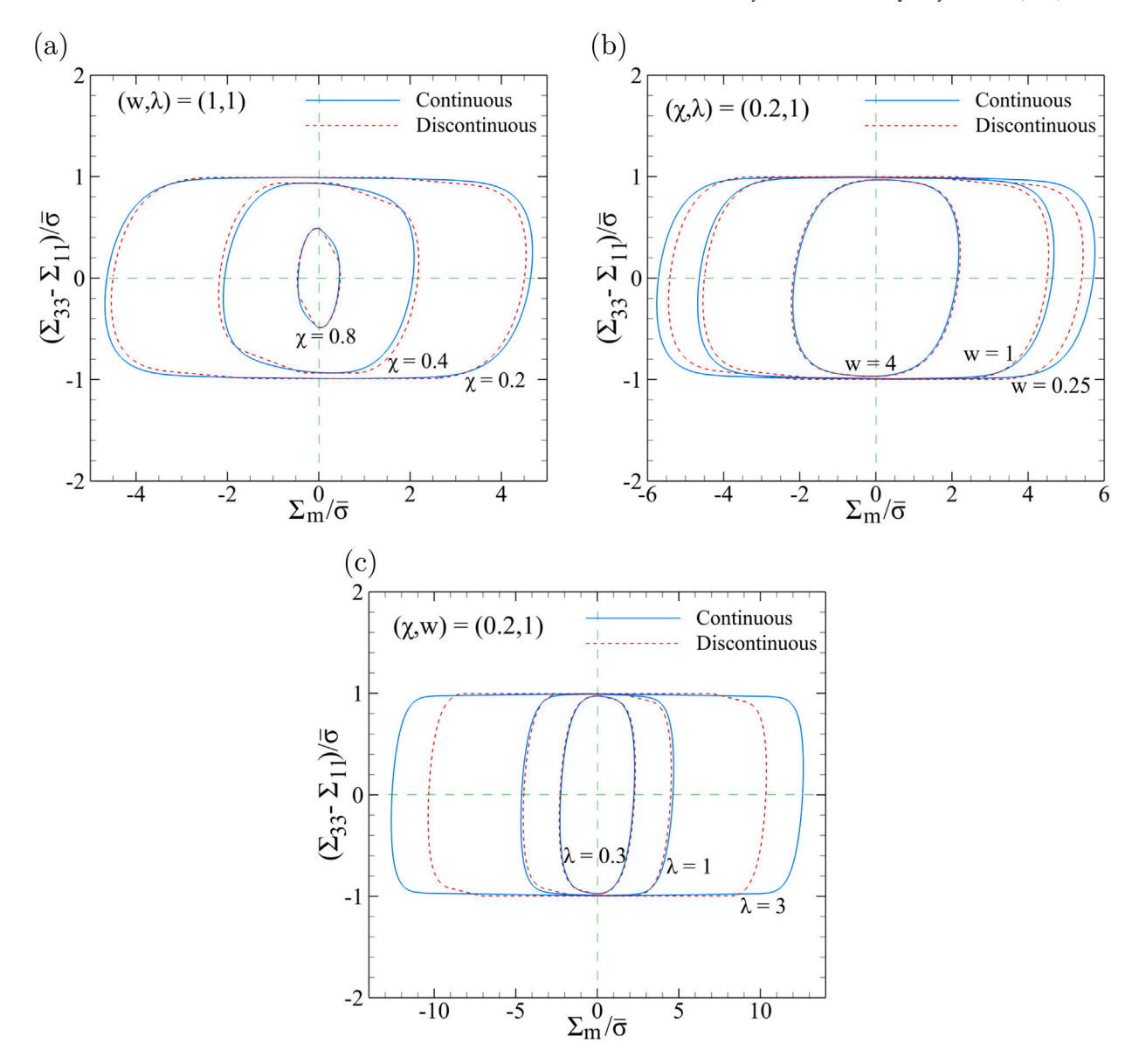


Fig. 8. Comparison between yield surfaces based on minimum and higher-continuity fields: (a) for fixed (w, λ) and various ligament parameters χ , (b) for fixed (χ, λ) and various void aspect ratios w, (c) for fixed (χ, w) and various cell aspect ratios λ .

and similar findings suggest that the new criterion provides a better estimate of the limit loads while preserving the upper-bound character.

Inevitably some differences between the two models are amenable to differing unit cells considered in the analysis. It is important to note that, unlike the new criterion, the earlier model in Gologanu et al. (2001b) does not preserve the upper-bound character because it considers an implicit velocity field that is approximate due to the inevitable geometry mismatch between a hollow cylinder and an ellipsoidal unit-cell. Also, the radius of the central porous zone in Gologanu et al. (2001b) is set by the condition of confocality of the inscribed spheroid with the spheroidal void, so that the volume fraction of the central zone is $c^{(p)} = \chi^2(w^2(1/c^2 - 1) + 1)$, which is not guaranteed to stay below 1 (e.g. for high values of χ). Furthermore, the relative porosity inside the central zone is $f^{(p)} = c \chi^2/c^{(p)}$, which tends to 2/3 when c goes to 1 (i.e. when coalescence in columns is complete). Yet, the value of 2/3 for $f^{(p)}$ is too high for the porous material plasticity model used inside the porous zone to remain valid.

4.3. Coalescence in columns versus layers

Whether coalescence in columns actually prevails over coalescence in layers or simply over void growth depends on the stress state and on internal parameters χ , w and λ . To analyze this, Fig. 10 shows, for various combinations of the internal parameters,

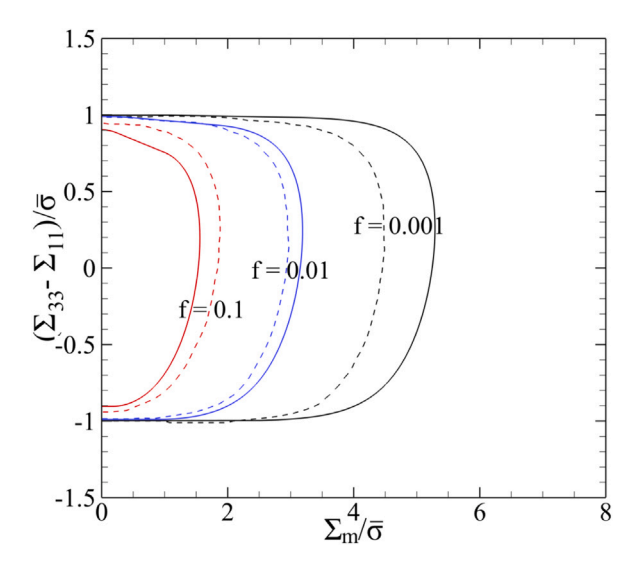


Fig. 9. Comparison between the present model predictions (solid lines) with those of Gologanu et al. (2001b) (dashed) for w = 1/2, $\lambda = 1/3$ and various values of the porosity f.

the surface predicted assuming coalescence in columns alone (broken line) as well as the surface predicted assuming either void growth or coalescence in layers, as predicted by the unified model of Morin et al. (dashed). The surface labeled "effective" is a hybrid surface that corresponds to the envelope (innermost surface). By construction, the effective surface contains corners at the junction between the parent two surfaces. Although the elementary cell used in both models is the same, the velocity fields that were employed differ from each other and this inevitably leads to corners. Whether such corners actually exist in the true surface is unknown.

For void and cell aspect ratios equal to unity (Fig. 10a and b) coalescence in columns is found to prevail over a very narrow range of stress states (wherever the solid line coincides with the broken line). That such a regime includes some cases of major (tensile) lateral stress has been known for a long time (Gologanu et al., 2001b). However, it is found here that even for a major axial stress (upper-right quadrant) coalescence in columns may be active, at least for the idealized cylindrical geometry considered in this work. When active, the regime of coalescence in layers is easily discernible in the form of flat inclined parts having a slope of -3/2. This is visible in both Fig. 10a and b.

If now an elongated void is embedded in a cell with unit aspect ratio, the entire effective surface may be determined by coalescence in columns. This is illustrated for w=3 in Fig. 10c where the "column coalescence" surface (broken lines) does not appear as it overlaps with the effective surface. The same observation holds if a void of unit aspect ratio is placed in a flat cell, as illustrated for $\lambda=0.5$ in Fig. 10d. In both cases, the ligament parameter χ was chosen so as to favor void coalescence over void growth.

More generally, coalescence in columns is the prevalent mechanism for slender matrices ($\chi \ge 0.3$), elongated voids (w > 2), and flat cells (for $\lambda \le 0.5$). Considering the axial ligament ratio $c = \chi w/\lambda$ coalescence in columns is favored for large values of c, irrespective of stress state.

It is emphasized that the above plots are provided for illustration purposes. The question of which regime dominates ultimately depends on the accuracy of each criterion. This is better assessed against putatively exact surfaces, as discussed in the next section.

4.4. Analytical versus computed surfaces

In Figs. 11–14 effective yield surfaces (solid lines) are assessed against computed ones (points) for various values of the internal parameters. Each computed surface contains up to 150 points. Each point on the computed surface corresponds to a separate finite element analysis following the method presented in Section 3.1. The surfaces corresponding to coalescence in columns (broken line) and unified model (dashed) are also shown so that the reader may easily identify the active mechanism. Recall that the active regime is that whose surface locally coincides with the effective surface.

For a void of unit aspect ratio in a cell of unit aspect ratio (Fig. 11) effective yielding is dominated by either void growth or coalescence in layers so long as the ligament parameter (or the overall porosity) is small. This is illustrated for $\chi=0.1$, which corresponds to f=0.001, Fig. 11a. The effective surface is somewhat far from the computed one for moderate to high triaxialities. However, as noted by Morin et al. (2015) the correspondence becomes near perfect if a Tvergaard-like parameter q is introduced in the void growth portion. This is not done here in order to keep the upper-bound character in the ensuing discussion.

As the ligament parameter is increased, the effective surface becomes a tighter upper bound; see the cases $\chi=0.4$ and $\chi=0.6$ in Fig. 11b and c. However, it is now noted that there are two regimes for which coalescence in columns prevails. The first regime

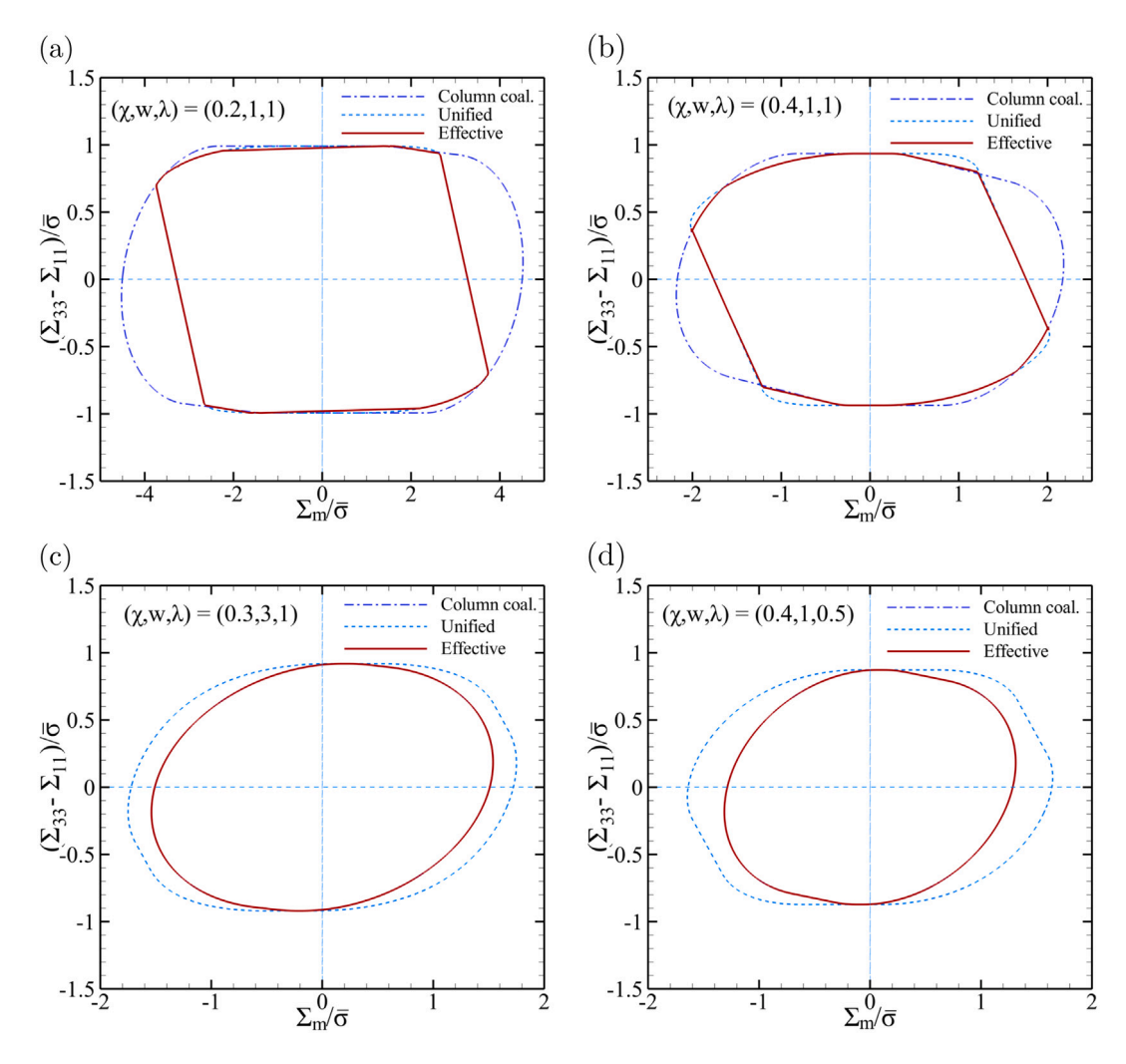


Fig. 10. Yield surfaces for coalescence in columns, criterion Eq. (40), versus coalescence in layers and void growth, unified criterion Eq. (49). The effective (hybrid) surface reveals the active yielding mechanism for a given stress state.

corresponds to stress states where the major stress is lateral ($\Sigma_{33} - \Sigma_{11} < 0$) and was identified by Gologanu et al. (1994b, 2001b) using unit cell calculations. The second regime corresponds to a major axial stress for low to moderate triaxialities. This regime was not identified by Gologanu et al. (1994b, 2001b). Fig. 12 depicts velocity field profiles within the cell representative of each of the two regimes above (parts (a) and (b)). By way of comparison, Fig. 12c shows an example of the velocity flow field corresponding to a state of coalescence in layers. Note in that case that the velocity is parallel to the boundary on the sides, which results from the pure uniaxial stretching mode characteristic of this regime.

Fig. 13 shows yield surfaces at fixed ligament parameter ($\chi = 0.25$) and unit cell aspect ratio ($\lambda = 1$) but for varying void aspect ratio. For voids with w = 1 (Fig. 13b) or flatter (Fig. 13a), coalescence in columns is unlikely as the broken-line surfaces lie very far from the computed ones. However, what is of interest is the w = 3 case, Fig. 13c. The propensity for coalescence in columns significantly increases for elongated voids and becomes dominant for w = 10 (not shown to avoid cluttering). This is consistent with experimental observations (Benzerga, 2000).

Similarly, Fig. 14 shows yield surfaces at fixed ligament parameter ($\chi=0.25$) and unit void aspect ratio (w=1) but for varying cell aspect ratio. For elongated cells (e.g. $\lambda=5$ in the figure) or cells of unit aspect ratio ($\lambda=1$) coalescence in columns is unlikely. Remarkably, however, for flatter cells (e.g. $\lambda=0.3$ in the figure) coalescence in columns becomes the dominant regime under *all* stress states; see Fig. 14a. Here, as in Fig. 10c, the "column coalescence" surface (broken line) is hidden by the effective surface, which is identified with it. What is even more remarkable is how tight the predicted column coalescence surface (solid line in Fig. 14a) is to the computed one (points). Recall that there is *no adjustable parameter* in the analytical criterion. Noting how far the dashed line (layer coalescence) is from the exact surface, this result is the most important practical finding of this investigation.

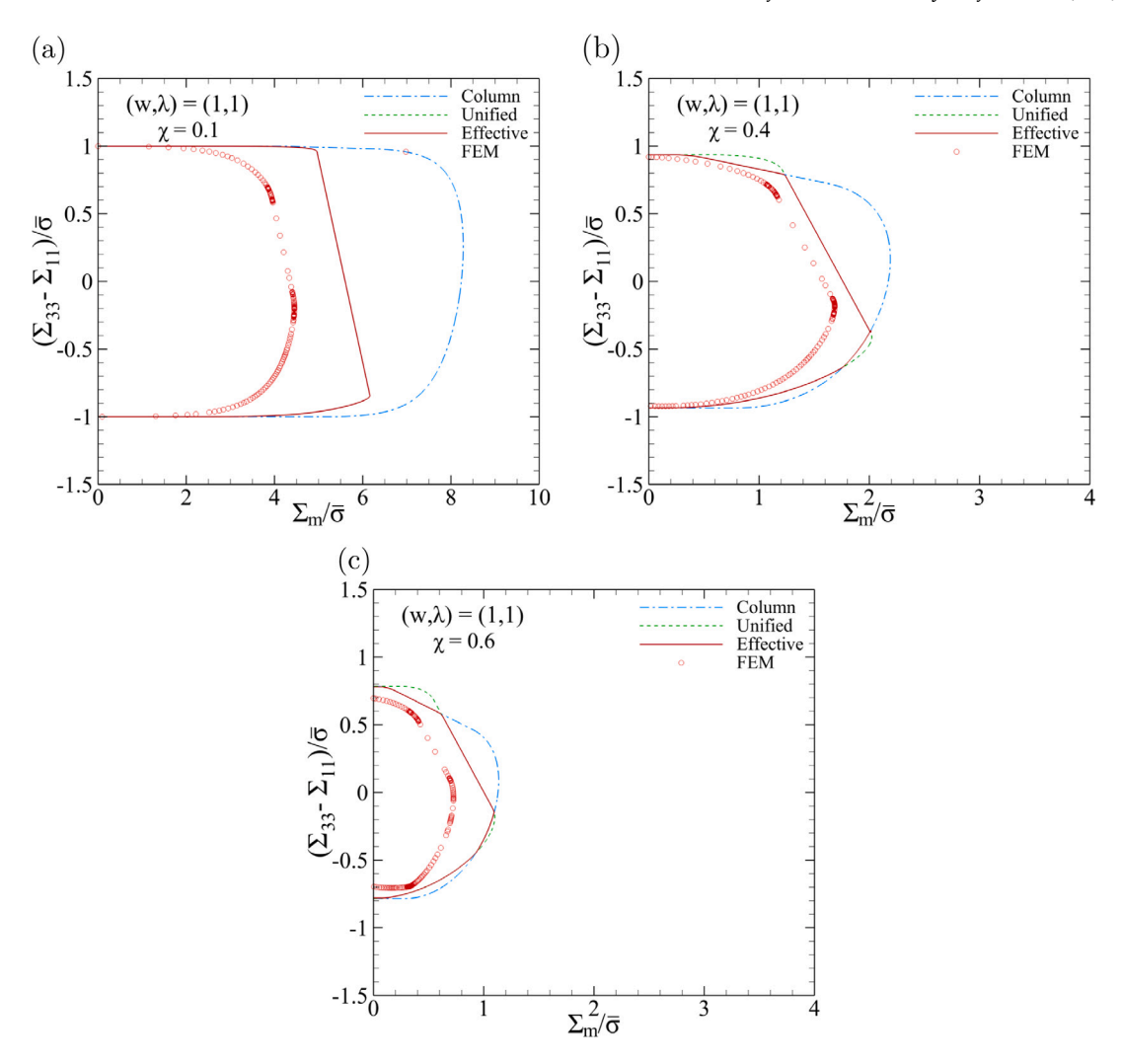


Fig. 11. Effective (analytical) versus computed (FEM) yield surfaces for fixed w and λ and various values of the ligament parameter: (a) $\chi=0.1$; (b) $\chi=0.4$; (c) $\chi=0.6$. In all, surfaces for coalescence in columns and coalescence in layers or void growth (unified) are shown for reference.

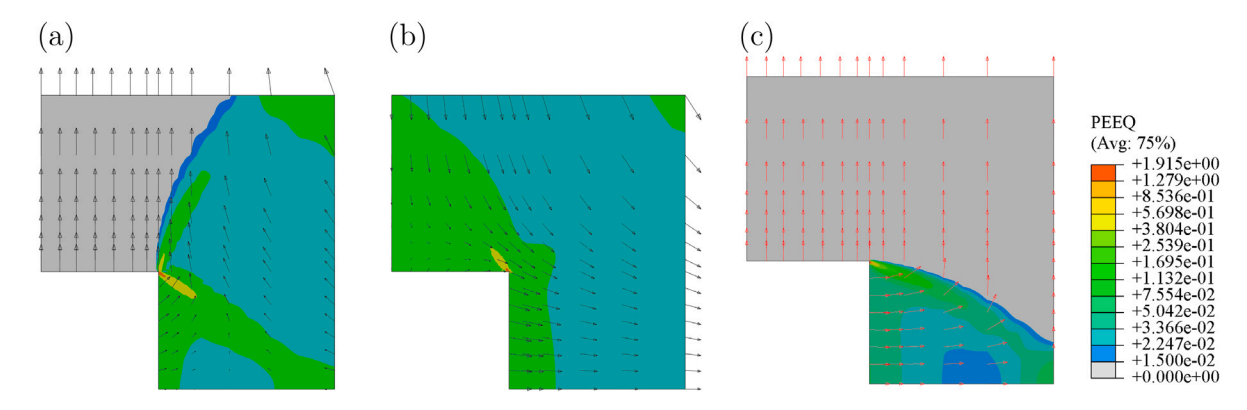


Fig. 12. Velocity fields superposed onto contours of equivalent plastic strain for (a) w=1, $\lambda=1$ and $\chi=0.4$ under (T,L)=(1,-1); (b) w=1, $\lambda=1$ and $\chi=0.4$ under (T,L)=(1,1); (c) w=1, $\lambda=1$ and $\chi=0.4$ under (T,L)=(2,-1). Cases (a) and (b) correspond to coalescence in columns and case (c) to coalescence in layers.

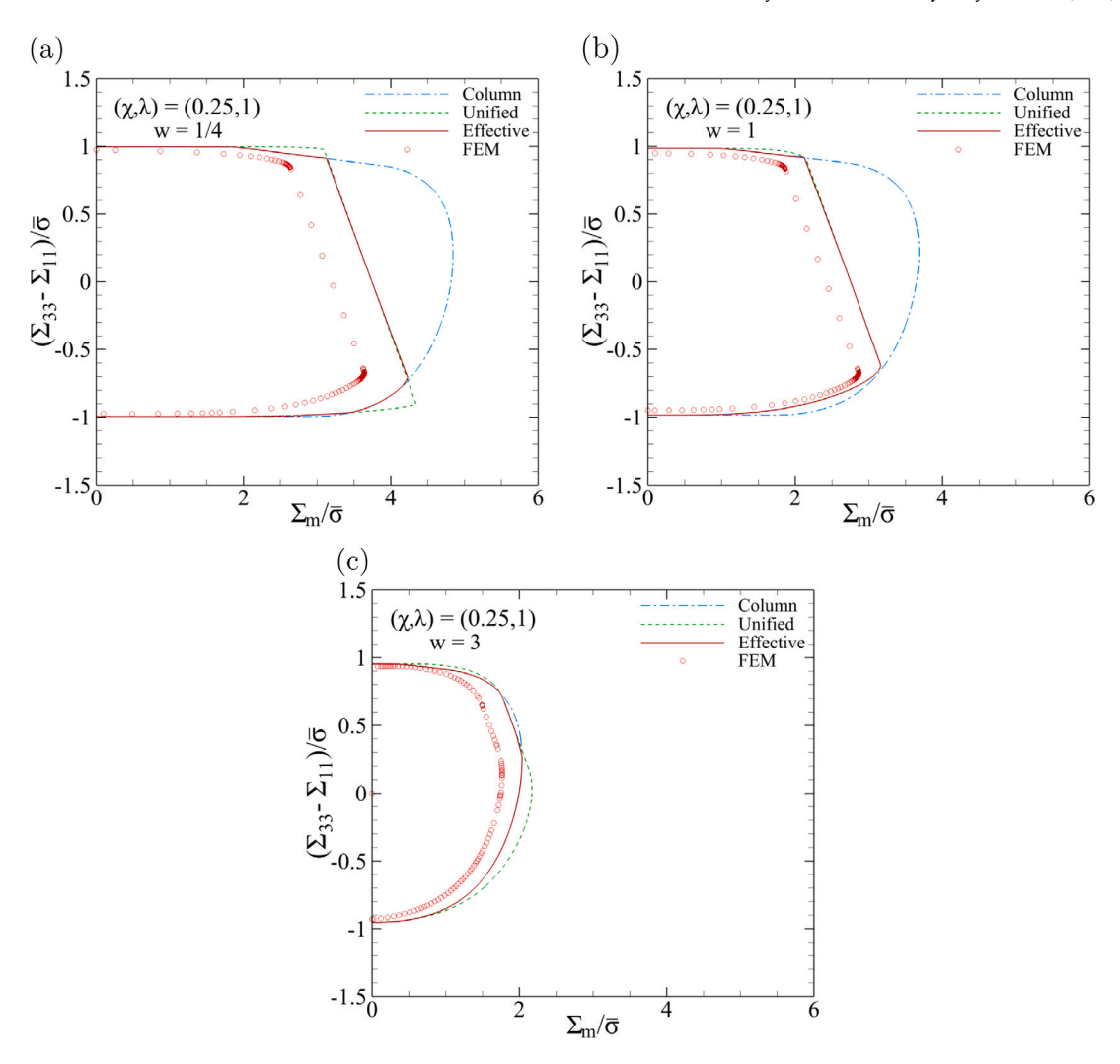


Fig. 13. Effective (analytical) versus computed (FEM) yield surfaces for fixed χ and λ and various values of the void aspect ratio: (a) w = 1/4; (b) w = 1; (c) w = 3. In all, surfaces for coalescence in columns and coalescence in layers or void growth (unified) are shown for reference.

Note in closing that when coalescence in layers is active, the limit load is insensitive to the value of λ . That the FEM results exhibit a markedly large effect of λ for flatter cells is therefore sufficient indication that coalescence in layers is inactive for that range of λ .

5. Conclusion

The phenomenon of void coalescence in columns (also known as necklace coalescence) has been treated analytically and numerically under axisymmetric loading conditions. The summary of findings is as follows:

- Void coalescence in columns is not restricted to regimes of major lateral stress. It can also be active under a major axial stress depending on the set of internal parameters.
- Circumstances under which coalescence in columns is favored include cases with elongated voids that are closely packed along their main axis, in keeping with experimental observations.
- When void coalescence in columns is active, it is remarkable how accurate an estimate the analytical yield criterion provides; see Figs. 13c and 14a.
- While most results have been presented using the criterion obtained with a discontinuous velocity field, an alternative yield criterion was also proposed. The latter has the considerable advantage of corresponding to a smooth yield surface, which is desirable for structural computations.
- There is a need to further enhance the model so as to:

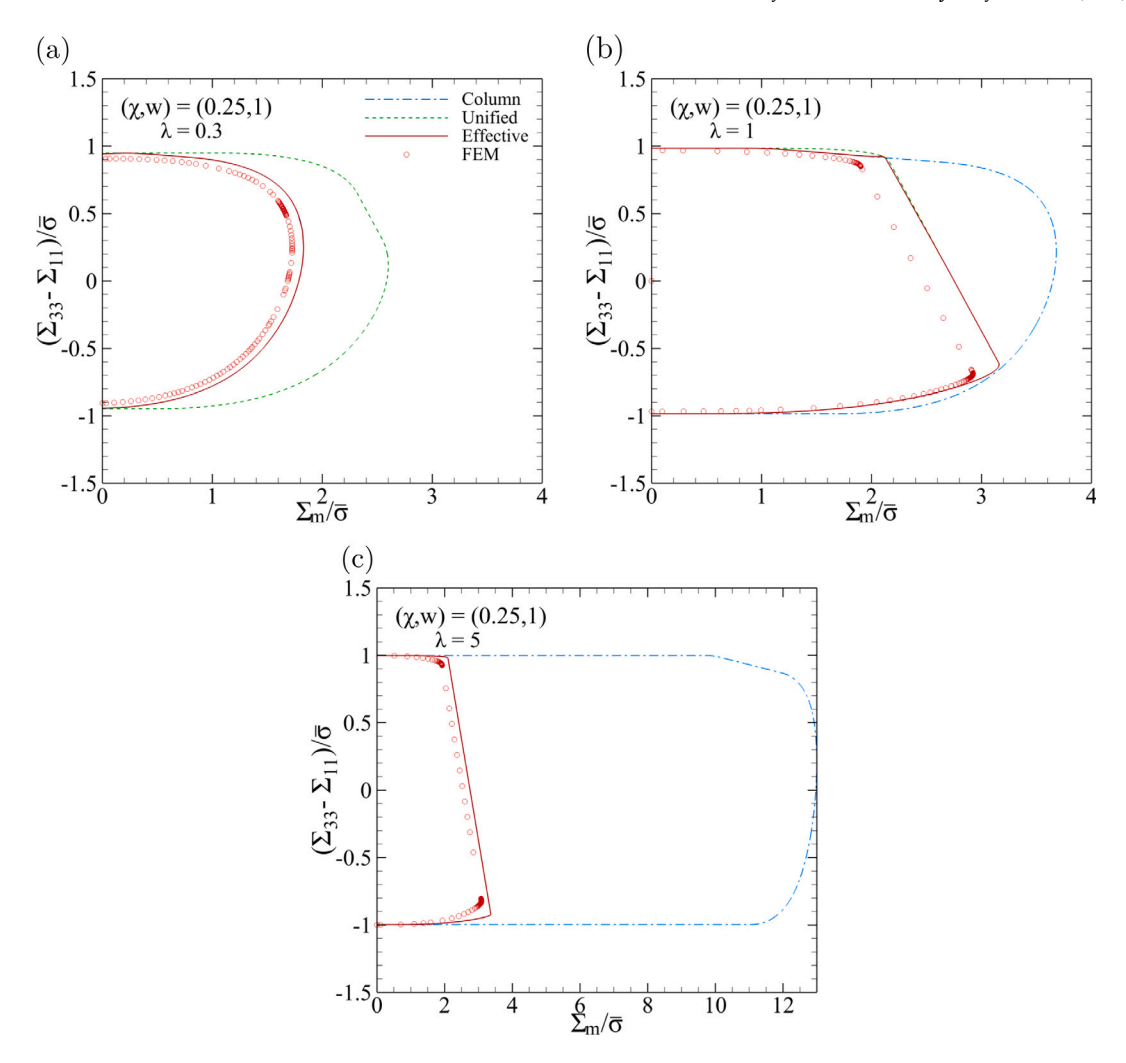


Fig. 14. Effective (analytical) versus computed (FEM) yield surfaces for fixed χ and w and various values of the cell aspect ratio: (a) $\lambda = 0.3$; (a) $\lambda = 1$; (a) $\lambda = 5$. In all, surfaces for coalescence in columns and coalescence in layers or void growth (unified) are shown for reference.

- develop evolution equations for the internal parameters;
- extend it to non-circular cylindrical geometries to enable the simplest extension to non-axisymmetric loadings.

CRediT authorship contribution statement

M.E. Torki: Designed the research, Developed the analytical models and prepared all figures, Contributed to the analysis of the results and to writing the paper. **F.A. Medrano:** Carried out the calculations. **A.A. Benzerga:** Designed the research, Contributed to the analysis of the results and to writing the paper. **J.-B. Leblond:** Designed the research, Contributed to the analysis of the results and to writing the paper.

Declaration of competing interest

The authors declare that they have no known competing financial interests or personal relationships that could have appeared to influence the work reported in this paper.

Data availability

Data will be made available on request.

Acknowledgments

This work was initiated with support from the National Science Foundation, USA under Grant Number CMMI-1405226. AAB acknowledges support from the National Science Foundation, USA (Grant Number CMMI-1932975). We are indebted to the anonymous reviewer whose remarks led us to significant improvements in the presentation.

Appendix A. Derivation of exact yield criterion Eq. (40)

It is recalled that the dissipation function given by Eq. (29) is non-differentiable owing to the presence of absolute values in the expressions Eq. (25) and Eq. (28) of $\Pi^{(P)}$ and Π^{surf} . Therefore, there are singular parts on the yield locus, which require a specific analysis differing from that of the regular parts.

The derivations follow the methodology first outlined by Torki et al. (2015) and later applied by Morin et al. (2016) and Torki et al. (2017). The fundamental inequality of limit analysis, Eq. (1), is rewritten for both pairs (D_{kk}, D_{33}) and $(-D_{kk}, -D_{33})$ so as to only consider non-negative values of D_{33} . The function $\Pi(D_{kk}, D_{33})$ being even one gets:

$$\forall D_{kk}, D_{33}, \quad D_{33} \geq 0 \qquad - \Pi(D_{kk}, D_{33}) \leq \Sigma_{11} D_{kk} + (\Sigma_{33} - \Sigma_{11}) D_{33} \leq \Pi(D_{kk}, D_{33}) \tag{A.1}$$

Now dividing all sides by D_{33} , one obtains the nondimensional counterpart of Eq. (1) as:

$$\forall \xi \in \mathbb{R} \qquad -g(\xi) \le f(\xi) \le g(\xi) \tag{A.2}$$

where, Π being positively homogeneous of degree 1, the functions f and g are given by:

$$f(\xi) = \sqrt{3}\Sigma_{11}\,\xi + \Sigma_{33} - \Sigma_{11}$$

$$g(\xi) = \Pi(\sqrt{3}\xi, 1)$$
(A.3)

with ξ defined in Eq. (19). For ease of reference, the explicit expression of the function $g(\xi)$ is given below:

$$\frac{1}{\bar{\sigma}}g(\xi) = |\xi| \left[\sqrt{1 + \left(\frac{U}{\xi}\right)^2} - \sinh^{-1}\left(\frac{\xi}{U}\right) \right]_{U=\chi^2}^1 + (1-c)|\sqrt{3}\xi - \chi^2| + w\frac{(1-c)^2}{c}|\xi|$$
(A.4)

Fig. A.1a provides schematic representations of the curves $\zeta = g(\xi)$ and $\zeta = -g(\xi)$ in a plane (ξ, ζ) . By way of comparison, curves corresponding to the differentiable dissipation obtained with the continuous velocity field are shown in Fig. A.1b.

The curves in Fig. A.1a possess the following properties:

- The representative curve of the function $\zeta = g(\xi)$ is convex. This follows from the convexity of the function $\Pi(D_{kk}, D_{33})$; see Appendix E in Morin et al. (2016) for a justification of this property.
- Since the expressions of $\Pi^{(P)}$ and $\Pi^{(surf)}$ in Eq. (25) and Eq. (28) are respectively proportional to $|D_{kk} \chi^2 D_{33}|$ and $|D_{kk}|$, the expression of $g(\xi)$ in Eq. (A.4) contains terms proportional to $|\sqrt{3}\xi \chi^2|$ and $|\xi|$. It follows that the curves $\zeta = g(\xi)$ and $\zeta = -g(\xi)$ have angular points at $\xi = 0$ and $\xi = \chi^2/\sqrt{3}$; except at these points the curves are smooth.
- The curves $\zeta = g(\xi)$ and $\zeta = -g(\xi)$ admit straight asymptotes for $\xi \to \pm \infty$; in addition, the asymptote to the curve $\zeta = -g(\xi)$ for $\xi \to +\infty$ (resp. $\xi \to -\infty$) coincides with the asymptote to the curve $\zeta = g(\xi)$ for $\xi \to -\infty$ (resp. $\xi \to +\infty$). The justification of these properties is similar to what was outlined in Appendix F of Morin et al. (2016).

On the other hand, the curve $\zeta = f(\xi)$ is a straight line parameterized by Σ_{11} and Σ_{33} .

It is then easy to discuss the inequalities in (A.2) graphically. In order for the pair $(\Sigma_{11}, \Sigma_{33})$ to belong to the *domain of reversibility*, the corresponding straight line $\zeta = f(\xi)$ must lie between the curves $\zeta = g(\xi)$ and $\zeta = -g(\xi)$ (see Fig. A.1). Thus, for this pair to lie on the *overall yield locus*, that is on the boundary of the reversibility domain, the straight line $\zeta = f(\xi)$ must meet one of the curves $\zeta = g(\xi)$, $\zeta = -g(\xi)$ at some point, *without crossing it* to satisfy (A.2). Owing to the point symmetry of the yield locus (with respect to the origin), one need only consider half of it and thus assume that the straight line $\zeta = f(\xi)$ meets the curve $\zeta = g(\xi)$ without crossing it. According to Fig. A.1 this may occur in three cases:

1. The straight line $\zeta = f(\xi)$ meets the curve $\zeta = g(\xi)$ at $\xi = 0$ and lies between the two tangents to this curve at this (angular) point, Fig. A.2a. Then the ordinate of the line at the origin is fixed, being equal to $f(0) = \Sigma_{33} - \Sigma_{11} = g(0)$, whereas its slope may vary between specific bounds, namely, $g'(0^-) \le f'(0) \le g'(0^+)$. Asymptotic analysis near $\xi = 0$ shows that the derivative of the first term of g in Eq. (A.4) vanishes such that:

$$\lim_{\xi \to 0^{\pm}} \frac{1}{\bar{\sigma}} g'(\xi) = -\sqrt{3}(1-c) \pm w \frac{(1-c)^2}{c}$$
(A.5)

In other words, there must be a straight (singular) portion on the yield locus, defined by:

$$\Sigma_{33} - \Sigma_{11} = \bar{\sigma}(1 - c\chi^2) \quad \text{for} \quad \left| \frac{\Sigma_{11}}{\bar{\sigma}} + (1 - c) \right| \le \frac{w}{\sqrt{3}} \frac{(1 - c)^2}{c}$$
 (A.6)

Fig. A.2b depicts the straight portion as two segments for convenience of plotting the yield surface in the half plane $\Sigma_{\rm m} \geq 0$.

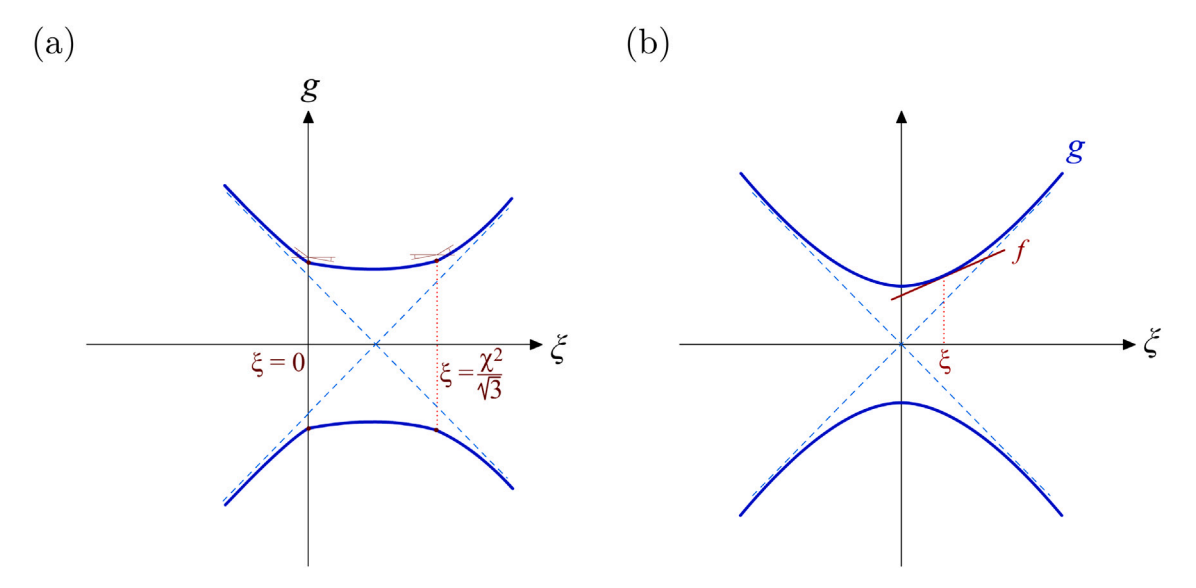


Fig. A.1. Schematic representation of normalized functions $g(\xi)$ and $-g(\xi)$ for (a) the "discontinuous" model as per Eq. (A.4); (b) the "continuous" model for reference

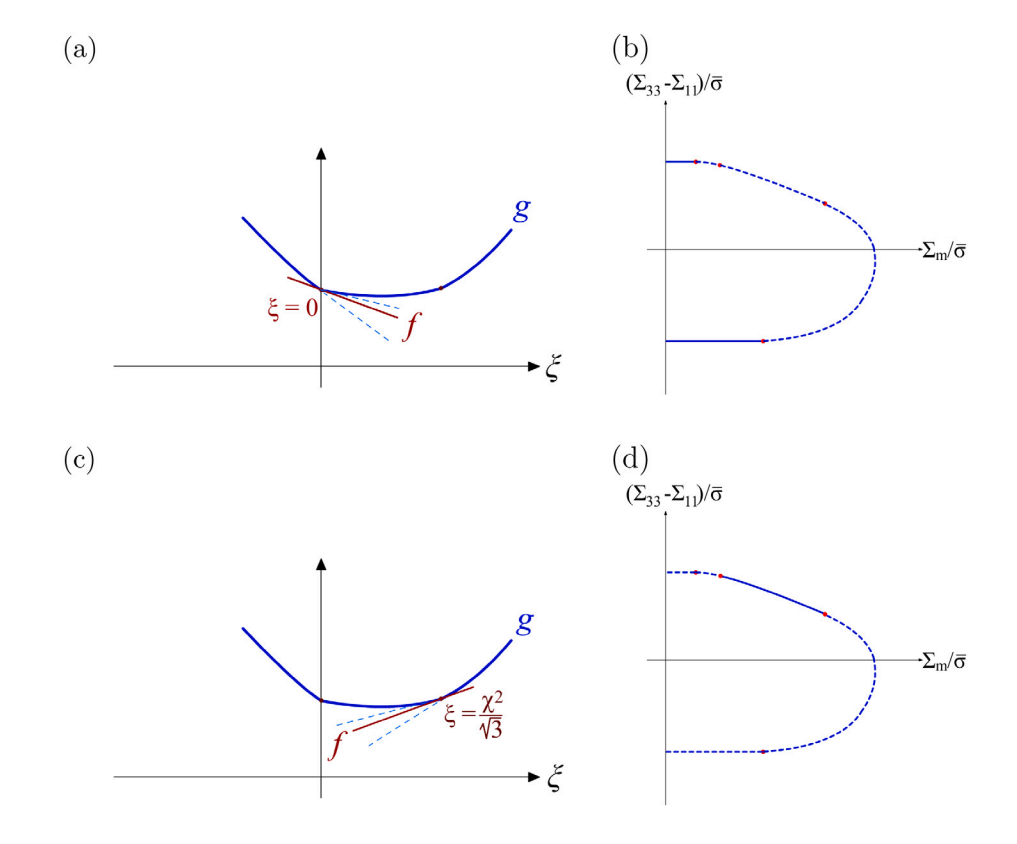


Fig. A.2. Graphical solution to Eq. (A.2). (a) Case of $\xi = 0$ leading to first type of singular parts on yield locus depicted in (b). (c) Case of $\xi = \chi^2/\sqrt{3}$ leading to second type of singular parts on yield locus depicted in (d).

2. The straight line $\zeta = f(\xi)$ meets the curve $\zeta = g(\xi)$ at $\xi = \chi^2/\sqrt{3}$ and lies between the two tangents to the curve at this point (see Fig. A.2c). Here too, the ordinate $f(\chi^2/\sqrt{3}) = \Sigma_{33} - (1 - \chi^2)\Sigma_{11}$ is fixed whereas its slope may vary between $g'(\chi^2/\sqrt{3})$

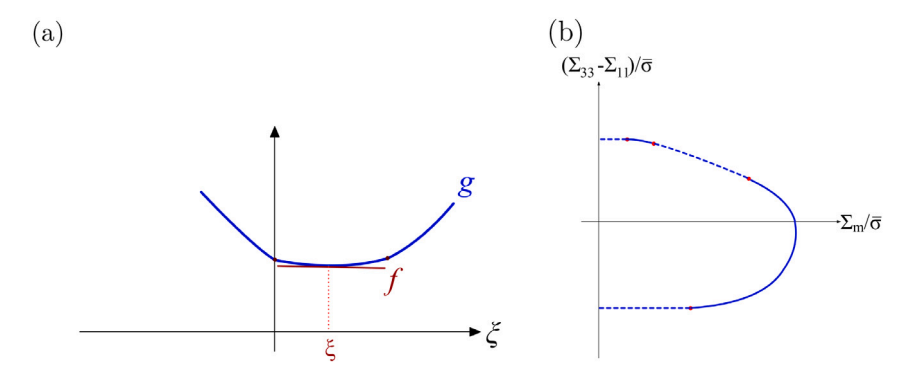


Fig. A.3. Graphical solution to Eq. (A.2). (a) Case of $\xi \neq 0, \xi \neq \chi^2/\sqrt{3}$ leading to regular, curved part on yield locus depicted in (b).

and $g'(\chi^2/\sqrt{3}^+)$. The following values are needed:

$$\frac{\sqrt{3}}{\bar{\sigma}}g\left(\frac{\chi^2}{\sqrt{3}}\right) = \sqrt{\chi^4 + 3} + \chi^2\left(\sinh^{-1}\frac{1}{\sqrt{3}} - 2\right) - \chi^2\sinh^{-1}\frac{\chi^2}{\sqrt{3}} + \chi^2w\frac{(1-c)^2}{c}$$
(A.7)

$$\frac{1}{\bar{\sigma}}g'\left(\frac{\chi^2}{\sqrt{3}}\right) = B \pm C \quad \text{with}$$
 (A.8)

$$B = \sinh^{-1} \frac{1}{\sqrt{3}} - \sinh^{-1} \left(\frac{\chi^2}{\sqrt{3}}\right) + w \frac{(1-c)^2}{c}$$

$$C = \sqrt{3}(1-c)$$
(A.9)

The other singular straight part of the yield locus is thus defined by (see Fig. A.2d):

$$(\Sigma_{33} - \Sigma_{11}) + \chi^2 \Sigma_{11} = A \quad \text{for} \quad \left| \frac{\Sigma_{11}}{\bar{\sigma}} - \frac{B}{\sqrt{3}} \right| \le \frac{C}{\sqrt{3}}$$
(A.10)

where $A \equiv g(\chi^2/\sqrt{3})$, B and C are given by Eqs. (A.7) and (A.9).

3. The straight line $\zeta = f(\xi)$ is tangent to the curve $\zeta = g(\xi)$ at some point lying neither at $\xi = 0$ nor at $\xi = \chi^2/\sqrt{3}$, Fig. A.3a. In this case, the ordinate of the line at the origin is a smooth function of its slope; this means that the stress point lies on the regular, curved part of the yield locus, Fig. A.3b.

In the latter case, Eq. (2) is applicable. Using Eq. (29), the yield locus is parametrically defined by:

$$\Sigma_{11} = \frac{\partial \Pi}{\partial D_{kk}} = \frac{\partial \Pi^{(M)}}{\partial D_{kk}} + \frac{\partial \Pi^{(P)}}{\partial D_{kk}} + \frac{\partial \Pi^{surf}}{\partial D_{kk}}$$

$$\Sigma_{33} - \Sigma_{11} = \frac{\partial \Pi}{\partial D_{33}} = \frac{\partial \Pi^{(M)}}{\partial D_{33}} + \frac{\partial \Pi^{(P)}}{\partial D_{33}} + \frac{\partial \Pi^{surf}}{\partial D_{33}}$$
(A.11)

Whether a discontinuous or a continuous velocity field is used, the first term in each equation is the same, given by Eq. (43). A classical manipulation (Benzerga and Leblond, 2010) leads to eliminating ξ from the two equations in (43) such that:

$$\left(\frac{\Sigma_{33}^{(M)} - \Sigma_{11}^{(M)}}{\bar{\sigma}}\right)^2 + 2\chi^2 \cosh\left(\sqrt{3}\frac{\Sigma_{11}^{(M)}}{\bar{\sigma}}\right) - 1 - \chi^4 = 0 \tag{A.12}$$

with the components of $\Sigma^{(M)}$ as defined by Eq. (42). Using the expressions of $\Pi^{(P)}$ and Π^{surf} , Eqs. (25) and (28), the remaining four terms in Eq. (A.11) are:

$$\begin{split} \frac{\partial \Pi^{(\mathrm{P})}}{\partial D_{kk}} = & (1-c)\bar{\sigma}\mathrm{sgn}\left(D_{kk} - \chi^2 D_{33}\right), & \frac{\partial \Pi^{\mathrm{surf}}}{\partial D_{kk}} = \frac{w}{\sqrt{3}} \frac{(1-c)^2}{c}\bar{\sigma}\mathrm{sgn}\left(D_{kk}\right) \\ \frac{\partial \Pi^{(\mathrm{P})}}{\partial D_{33}} = & -(1-c)\chi^2\bar{\sigma}\mathrm{sgn}\left(D_{kk} - \chi^2 D_{33}\right), & \frac{\partial \Pi^{\mathrm{surf}}}{\partial D_{33}} = 0 \end{split} \tag{A.13}$$

Then substituting for $\Sigma_{11}^{(M)}$ and $\Sigma_{33}^{(M)}$ their expressions given by Eq. (A.11) into Eq. (A.12) with due account for Eq. (A.13) delivers the final expression for the regular portion of the yield locus:

$$\left[\frac{\Sigma_{33} - \Sigma_{11}}{\bar{\sigma}} + \epsilon_1 (1 - c) \chi^2\right]^2 + 2\chi^2 \cosh\left[\sqrt{3} \frac{\Sigma_{11}}{\bar{\sigma}} - \epsilon_1 \sqrt{3} (1 - c) - \epsilon_2 w \frac{(1 - c)^2}{c}\right] - 1 - \chi^4 = 0 \tag{A.14}$$

with $\epsilon_1 = \text{sgn}(D_{kk} - \chi^2 D_{33})$ and $\epsilon_2 = \text{sgn}(D_{kk})$ giving rise to four distinct regular portions of the yield locus, two of which are represented in Fig. A.3.

On the other hand, Eqs. (A.6) and (A.10) only determine two segments of the singular parts. The other two are obtained by point symmetry, hence the general forms given in Eq. (40).

Appendix B. Details pertaining to the "continuous" model

The case $\Delta < 0$ in Eq. (36) corresponds to the situation where

$$\left[\frac{13}{12} - (\delta - 1)^2\right]\bar{\xi}^2 - 2\delta\left(\delta + \frac{1}{12}\right)\bar{\xi} + \frac{1}{12} < 0 \tag{B.1}$$

which is affected by the sign of the factor multiplying $\bar{\xi}^2$, namely:

$$\Delta < 0 \text{ if } \begin{cases}
\min \left(\bar{\xi}^{(1)}, \bar{\xi}^{(2)} \right) < \bar{\xi} < \max \left(\bar{\xi}^{(1)}, \bar{\xi}^{(2)} \right) \text{ for } \delta < 1 + \sqrt{\frac{13}{12}} \\
\bar{\xi} < \min \left(\bar{\xi}^{(1)}, \bar{\xi}^{(2)} \right) \quad \text{or} \quad \bar{\xi} > \max \left(\bar{\xi}^{(1)}, \bar{\xi}^{(2)} \right) \text{ for } \delta > 1 + \sqrt{\frac{13}{12}}
\end{cases} \tag{B.2}$$

where

$$(\bar{\xi}^{(1)}, \bar{\xi}^{(2)}) = \frac{1}{C} \left[1 \pm \sqrt{1 - \frac{1}{12}C} \right]$$
 (B.3)

with $C = \frac{13/12 - (\delta - 1)^2}{\delta + 1/12}$. Alternatively, condition Eq. (B.2) can also be expressed in the following form:

$$\Delta < 0 \text{ if } \begin{cases} \min\left(\bar{\xi}^{(1)}, \bar{\xi}^{(2)}\right) < \bar{\xi} < \max\left(\bar{\xi}^{(1)}, \bar{\xi}^{(2)}\right) \text{ for } v > 1 - 1.75\frac{\chi}{\lambda} \\ \bar{\xi} < \min\left(\bar{\xi}^{(1)}, \bar{\xi}^{(2)}\right) \quad \text{or} \quad \bar{\xi} > \max\left(\bar{\xi}^{(1)}, \bar{\xi}^{(2)}\right) \text{ for } v < 1 - 1.75\frac{\chi}{\lambda}, \ c < 1 - 1.75\frac{\chi}{\lambda} \end{cases}$$
(B.4)

where use has been made of Eq. (33)₂ and the fact that $c \le v \le 1$. Hence the second condition is not satisfied if $1 - 1.75\chi/\lambda < c$. Altogether, the integral in Eq. (34) should be split so as to exclude the range $v > 1 - 1.75 \chi/\lambda$ if Eq. (B.4)₁ is met, or the range $v < 1 - 1.75 \chi/\lambda$, $c < 1 - 1.75 \chi/\lambda$ if Eq. (B.4)₂ is met.

Appendix C. Yield criterion of Gologanu (1997)

The (axisymmetric) yield criterion for coalescence in columns developed by Gologanu et al. (2001b) is expressed in parametric form following Gologanu (1997):

$$\frac{\Sigma_{11}}{\bar{\sigma}} = -(1 - 2\alpha_2)\varepsilon \mathcal{A} + \left[1 + \eta(1 - 2\alpha_2)\right] \mathcal{B} + \mathcal{B}^*$$

$$\frac{\Sigma_{33}}{\bar{\sigma}} = -(1 - 2\alpha_2 - c)\varepsilon \mathcal{A} + \left[1 + \eta(1 - 2\alpha_2 - c)\right] \mathcal{B} + \operatorname{sgn}\left(D_{33}\right) \mathcal{A}^* + \mathcal{B}^*$$
(C.1)

where

$$\mathcal{A} = \frac{1}{\sqrt{C}} \left(\sqrt{\Lambda^2 + (g+1)^2} - \sqrt{\Lambda^2 + q_1^2 (g+f)^2} \right)$$

$$\mathcal{B} = \frac{1}{\kappa} \left(\sinh^{-1} \frac{\Lambda}{q_1 (g+f)} - \sinh^{-1} \frac{\Lambda}{g+1} \right)$$
(C.2)

with

$$\varepsilon = \operatorname{sgn}(D_{33})\operatorname{sgn}\left(c - \sqrt{3}\operatorname{sgn}(D_{33})\Lambda^*(1 - 2\alpha_2)\right)$$

$$\Lambda = \frac{\sqrt{C}}{\varepsilon \kappa} \left[\frac{\sqrt{3}\operatorname{sgn}(D_{33})\Lambda^*}{c - \sqrt{3}\operatorname{sgn}(D_{33})\Lambda^*(1 - 2\alpha_2)} - \eta \right]$$
(C.3)

and

$$A^* = \sqrt{A^{*2} + 1} - \sqrt{A^{*2} + c^2}$$

$$B^* = \frac{1}{\sqrt{3}} \left(\sinh^{-1} \frac{A^*}{c} - \sinh^{-1} A^* \right)$$
(C.4)

with

$$A^* = \frac{1}{\sqrt{3} \text{sgn}(D_{33})} \frac{\text{tr}(\mathbf{D})}{D_{33}}$$

The remaining parameters that appear in the above equations, namely α_2 , η , C, g and κ enter the void growth criterion of Gologanu et al. (1997) which was used in deriving the model of coalescence in columns using their two-step homogenization approach. Finally, q_1 is Tvergaard's parameter, here taken to be unity.

References

Barrioz, P.O., Hure, J., Tanguy, B., 2019. On void shape and distribution effects on void coalescence. J. Appl. Mech. 86, 0110061.

Benzerga, A.A., 2000. Rupture Ductile Des Tôles Anisotropes (Ph.D. thesis). Ecole Nationale Supérieure des Mines de Paris.

Benzerga, A.A., 2002. Micromechanics of coalescence in ductile fracture. J. Mech. Phys. Solids 50, 1331-1362.

Benzerga, A.A., Leblond, J.B., 2010. Ductile fracture by void growth to coalescence. Adv. Appl. Mech. 44, 169-305.

Benzerga, A.A., Leblond, J.B., 2014. Effective yield criterion accounting for microvoid coalescence. J. Appl. Mech. 81, 031009.

Drucker, D.C., Prager, W., Greenberg, M.J., 1952. Extended limit analysis theorems for continuous media. Q. Appl. Math. 9, 381-389.

Gologanu, M., 1997. Etude de Quelques Problèmes de Rupture Ductile Des Métaux (Ph.D. thesis). Université Paris, p. 6.

Gologanu, M., Leblond, J.B., Devaux, J., 1994a. Approximate models for ductile metals containing non-spherical voids — Case of axisymmetric oblate ellipsoidal cavities. J. Eng. Mater. Technol. 116, 290–297.

Gologanu, M., Leblond, J.B., Devaux, J., 1994b. Numerical and theoretical study of coalescence of cavities in periodically voided solids. In: Noor, A.K., Needleman, A. (Eds.), Computational Material Modeling, Vol. AD-42/PVP-294. ASME, New York, pp. 223–244.

Gologanu, M., Leblond, J.B., Perrin, G., Devaux, J., 1997. Recent extensions of gurson's model for porous ductile metals. In: Suquet, P. (Ed.), Continuum Micromechanics. In: CISM Lectures Series, Springer, New York, pp. 61–130.

Gologanu, M., Leblond, J.B., Perrin, G., Devaux, J., 2001a. Theoretical models for void coalescence in porous ductile solids – I: Coalescence in layers. Int. J. Solids Struct. 38, 5581–5594.

Gologanu, M., Leblond, J.B., Perrin, G., Devaux, J., 2001b. Theoretical models for void coalescence in porous ductile solids – II: Coalescence in columns. Int. J. Solids Struct. 38, 5595–5604.

Gradshtein, I.S., Ryzhik, I.M., 1971. Tables of integrals, sums, series and products.

Gurson, A.L., 1977. Continuum theory of ductile rupture by void nucleation and growth: Part I- yield criteria and flow rules for porous ductile media. J. Eng. Mater. Technol. 99, 2-15.

Hure, J., Barrioz, P.O., 2016. Theoretical estimates for flat voids coalescence by internal necking. Eur. J. Mech. 60, 217-226.

Keralayarma, S.M., Chockalingam, S., 2016. A criterion for void coalescence in anisotropic ductile materials. Int. J. Plast. 82, 159-176.

Koplik, J., Needleman, A., 1988. Void growth and coalescence in porous plastic solids. Int. J. Solids Struct. 24, 835-853.

Leblond, J.B., Kondo, D., Morin, L., Remmal, A., 2018. Classical and sequential limit analysis revisited. C. R. Mec. 346, 336-349.

Madou, K., Leblond, J.B., 2012. A gurson-type criterion for porous ductile solids containing arbitrary ellipsoidal voids – II: Determination of yield criterion parameters. J. Mech. Phys. Solids 60, 1037–1058.

Madou, K., Leblond, J.B., 2013. Numerical studies of porous ductile materials containing arbitrary ellipsoidal voids — I: Yield surfaces of representative cells. Eur. J. Mech. 42, 480–489.

Morin, L., Leblond, J.B., Benzerga, A.A., 2015. Coalescence of voids by internal necking: theoretical estimates and numerical results. J. Mech. Phys. Solids 75, 140–158.

Morin, L., Leblond, J.B., Benzerga, A.A., Kondo, D., 2016. A unified criterion for the growth and coalescence of microvoids. J. Mech. Phys. Solids 97, 19-36.

Morin, L., Michel, J.C., 2018. Void coalescence in porous ductile solids containing two populations of cavities. Eur. J. Mech. 72, 341-353.

Pardoen, T., Hutchinson, J.W., 2000. An extended model for void growth and coalescence. J. Mech. Phys. Solids 48, 2467-2512.

Tekoğlu, C., Leblond, J.B., Pardoen, T., 2012. A criterion for the onset of void coalescence under combined tension and shear. J. Mech. Phys. Solids 60, 1363-1381.

Thomason, P.F., 1985. Three-dimensional models for the plastic limit-loads at incipient failure of the intervoid matrix in ductile porous solids. Acta Metall. 33, 1079–1085.

Torki, M.E., 2019. A unifed criterion for void growth and coalescence under combined tension and shear. Int. J. Plast. 119, 57-84.

Torki, M.E., Benzerga, A.A., 2018. A mechanism of failure in shear bands. Extreme Mech. Lett. 23, 67-71.

Torki, M.E., Benzerga, A.A., 2022. Ductile fracture in plane stress. J. Appl. Mech. 89, 011001.

Torki, M.E., Benzerga, A.A., Leblond, J.B., 2015. On void coalescence under combined tension and shear. J. Appl. Mech. 82, 071005.

Torki, M.T., Keralavarma, S.M., Benzerga, A.A., 2021. An analysis of Lode effects in ductile failure. J. Mech. Phys. Solids 153, 104468.

Torki, M.E., Tekoglu, C., Leblond, J.B., Benzerga, A.A., 2017. Theoretical and numerical analysis of void coalescence in porous ductile solids under arbitrary loadings. Int. J. Plast. 91, 160–181.

Trillat, M., Pastor, J., 2005. Limit analysis and Gurson's model. Eur. J. Mech. 24, 800-819.

Tvergaard, V., 1982. On localization in ductile materials containing spherical voids. Int. J. Fract. 18, 237–252.